



Global methane emission estimates for 2000–2012 from CarbonTracker Europe-CH₄ v1.0

Aki Tsuruta¹, Tuula Aalto¹, Leif Backman¹, Janne Hakkarainen², Ingrid T. van der Laan-Luijkx^{3,5}, Maarten C. Krol^{3,4,5}, Renato Spahni⁶, Sander Houweling^{4,5}, Marko Laine², Ed Dlugokencky⁷, Angel J. Gomez-Pelaez⁸, Marcel van der Schoot⁹, Ray Langenfelds⁹, Raymond Ellul¹⁰, Jgor Arduini^{11,12}, Francesco Apadula¹³, Christoph Gerbig¹⁴, Dietrich G. Feist¹⁴, Rigel Kivi¹⁵, Yukio Yoshida¹⁶, and Wouter Peters^{3,17}

¹Climate Research, Finnish Meteorological Institute, Helsinki, Finland

²Earth Observation, Finnish Meteorological Institute, Helsinki, Finland

³Meteorology and Air Quality, Wageningen University & Research, Wageningen, the Netherlands

⁴SRON Netherlands Institute for Space Research, Utrecht, the Netherlands

⁵Institute for Marine and Atmospheric Research, Utrecht University, Utrecht, the Netherlands

⁶Climate and Environmental Physics, Physics Institute, and Oeschger Centre for Climate Change Research, University of Bern, Bern, Switzerland

⁷NOAA Earth System Research Laboratory, Global Monitoring Division, Boulder, Colorado, USA

⁸Izaña Atmospheric Research Center, Agencia Estatal de Meteorología (AEMET), Tenerife, Spain

⁹CSIRO Oceans and Atmosphere, Aspendale, Australia

¹⁰Atmospheric Research, Department of Geosciences, University of Malta, Msida, Malta

¹¹Department of Pure and Applied Sciences, University of Urbino, Urbino, Italy

¹²National Research Council, Institute of Atmospheric Sciences and Climate, Bologna, Italy

¹³Ricerca sul Sistema Energetico – RSE SpA, Milano, Italy

¹⁴Max Planck Institute for Biogeochemistry, Jena, Germany

¹⁵Arctic Research, Finnish Meteorological Institute, Sodankylä, Finland

¹⁶Center for Global Environmental Research, National Institute for Environmental Studies, Tsukuba, Ibaraki, Japan

¹⁷University of Groningen, Centre for Isotope Research, Groningen, the Netherlands

Correspondence to: Aki Tsuruta (aki.tsuruta@fmi.fi)

Received: 21 July 2016 – Discussion started: 19 August 2016

Revised: 17 February 2017 – Accepted: 21 February 2017 – Published: 27 March 2017

Abstract. We present a global distribution of surface methane (CH₄) emission estimates for 2000–2012 derived using the CarbonTracker Europe-CH₄ (CTE-CH₄) data assimilation system. In CTE-CH₄, anthropogenic and biospheric CH₄ emissions are simultaneously estimated based on constraints of global atmospheric in situ CH₄ observations. The system was configured to either estimate only anthropogenic or biospheric sources per region, or to estimate both categories simultaneously. The latter increased the number of optimizable parameters from 62 to 78. In addition, the differences between two numerical schemes available to perform turbulent vertical mixing in the atmospheric transport model TM5 were examined. Together,

the system configurations encompass important axes of uncertainty in inversions and allow us to examine the robustness of the flux estimates. The posterior emission estimates are further evaluated by comparing simulated atmospheric CH₄ to surface in situ observations, vertical profiles of CH₄ made by aircraft, remotely sensed dry-air total column-averaged mole fraction (XCH₄) from the Total Carbon Column Observing Network (TCCON), and XCH₄ from the Greenhouse gases Observing Satellite (GOSAT). The evaluation with non-assimilated observations shows that posterior XCH₄ is better matched with the retrievals when the vertical mixing scheme with faster interhemispheric exchange is used. Estimated posterior mean total global emis-

sions during 2000–2012 are $516 \pm 51 \text{ Tg CH}_4 \text{ yr}^{-1}$, with an increase of $18 \text{ Tg CH}_4 \text{ yr}^{-1}$ from 2000–2006 to 2007–2012. The increase is mainly driven by an increase in emissions from South American temperate, Asian temperate and Asian tropical TransCom regions. In addition, the increase is hardly sensitive to different model configurations ($< 2 \text{ Tg CH}_4 \text{ yr}^{-1}$ difference), and much smaller than suggested by EDGAR v4.2 FT2010 inventory ($33 \text{ Tg CH}_4 \text{ yr}^{-1}$), which was used for prior anthropogenic emission estimates. The result is in good agreement with other published estimates from inverse modelling studies ($16\text{--}20 \text{ Tg CH}_4 \text{ yr}^{-1}$). However, this study could not conclusively separate a small trend in biospheric emissions (-5 to $+6.9 \text{ Tg CH}_4 \text{ yr}^{-1}$) from the much larger trend in anthropogenic emissions ($15\text{--}27 \text{ Tg CH}_4 \text{ yr}^{-1}$). Finally, we find that the global and North American CH_4 balance could be closed over this time period without the previously suggested need to strongly increase anthropogenic CH_4 emissions in the United States. With further developments, especially on the treatment of the atmospheric CH_4 sink, we expect the data assimilation system presented here will be able to contribute to the ongoing interpretation of changes in this important greenhouse gas budget.

1 Introduction

Methane (CH_4) is a greenhouse gas with global warming potential 28 times that of carbon dioxide (CO_2) on a 100-year time horizon (Azar and Johansson, 2012; Boucher, 2012; Peters et al., 2011; Reisinger et al., 2010). Following years of almost no growth during 1999–2006, atmospheric CH_4 started to increase again in 2007 (Rigby et al., 2008; Dlugokencky et al., 2009). The growth rate of globally averaged atmospheric CH_4 from 2007 to 2012 was 5.7 ppb per year, which represents a significant change to the global CH_4 budget. The mechanisms behind this increase are still debated (e.g. Heiman, 2011; Dlugokencky et al., 2011; Dalsøren et al., 2016).

Methane is mainly emitted by anthropogenic activities and natural biogenic processes, followed by minor contributions from biomass burning, oceans, inland water bodies and geologic activities. The main anthropogenic sources are fugitive emission from solid fuels, leaks from gas extraction and distribution, agriculture, and waste management. Anthropogenic CH_4 emissions account for more than half of total CH_4 emissions from land and oceans (Kirschke et al., 2013; Saunio et al., 2016). Anthropogenic CH_4 emissions have increased significantly since preindustrial times largely due to the heavy use of fossil fuels, but also due to the increase in ruminants, landfills and rice fields corresponding to the increase in human population (Ghosh et al., 2015). This has resulted in a steep increase in the amount of CH_4 in the atmosphere. Previous studies suggest that anthropogenic CH_4 emissions did not increase significantly, or even decreased,

during the 1980s and 1990s (Bousquet et al., 2006; Dlugokencky et al., 1998), which may have been one of the causes of stabilization of the atmospheric CH_4 burden from 1999 to 2006 (Dlugokencky et al., 2003). Although the changes in CH_4 emissions in more recent years have not been satisfactorily explained, recent studies indicate an increase in the CH_4 emissions from biogenic sources (Schaefer et al., 2016; Schwietzke et al., 2016; Nisbet et al., 2016) and large CH_4 emissions from the tropics in the 21st century (Saunio et al., 2016). Methane emissions from natural wetlands account for around 30 % of total CH_4 emissions (Kirschke et al., 2013). Wetlands and peatlands are the major sources of natural biospheric CH_4 emissions. Most peatlands are in high northern latitudes, whereas large wetland areas are located in the tropics. Emissions from natural biospheric sources have strong seasonal and interannual variability (Spahni et al., 2011), contributing substantially to seasonal and interannual variability in the atmospheric CH_4 burden (Meng et al., 2015). In addition, photochemical reaction with hydroxyl (OH) in the troposphere, the major sink of CH_4 , has strong effects on the annual cycle of atmospheric CH_4 .

Attributing the observed changes in CH_4 burden to changes in emission sources is difficult because variations in CH_4 emissions from both anthropogenic and biogenic sources are not sufficiently understood. In addition, considerable uncertainty remains on changes in the lifetime of atmospheric CH_4 . Montzka et al. (2011) found an increase in OH concentrations in the beginning of the 21st century, followed by a decrease in OH concentrations after 2004–2005. More recently, Ghosh et al. (2015) and Dalsøren et al. (2016) also obtained a decrease in the CH_4 lifetime in their simulations. McNorton et al. (2016) showed that although interannual variability of OH may be small, small changes in OH concentrations could lead to significant changes in CH_4 concentrations. On the other hand, Rigby et al. (2008) suggested that a decrease in tropospheric OH concentration could be one of the reasons for the increase in atmospheric CH_4 after 2007. The uncertainty in changes in OH concentrations and its relation to the CH_4 burden still remains large (Prather et al., 2012), and needs to be further assessed.

Several inverse models have been developed to estimate CH_4 emissions and their contribution to the atmospheric CH_4 burden (e.g. Bousquet et al., 2006; Bruhwiler et al., 2014; Houweling et al., 2014; Fraser et al., 2013; Meirink et al., 2008). Emission estimates vary among models (e.g. Kirschke et al., 2013; Locatelli et al., 2013; Bergamaschi et al., 2015; Tsuruta et al., 2015) as these inverse systems rely on specific choices in the design of the inverse problem. Inputs, such as prior emission fields and observations, and the transport model used in inversions play a major role in regional and continental emission estimates. Depending on the optimization method and available information, it may or may not be possible to derive information at small spatial scales. For example, the computational cost in adjoint models (Bergamaschi et al., 2015; Belikov et al., 2013; Houweling et al.,

2014; Meirink et al., 2008) is not highly dependent on the number of scaling factors used to “scale” the prior (first guess of emission estimates) in order to get optimized (posterior) emissions, i.e. such models have the ability to perform grid-scale optimization globally. The computational cost in some other methods, such as in Thompson and Stohl (2014) and Zhao et al. (2009) depend on the number of scaling factors as the method directly uses their very large covariance matrix. In that case, grid-scale optimization is possible without any asymptotic assumptions, but only for regional domains, because the dimensions of the covariance matrix for a global domain become too large, even for current computational capability. Ensemble Kalman filter (EnKF)-based systems (Bruhwiler et al., 2014; Tsuruta et al., 2015) typically have smaller computational limitations related to the number of scaling factors. By representing the state covariance matrix with a limited number of samples of the state (ensemble members), the computational cost depends mostly on the number of ensemble members. The trade-off in these methods comes as an approximation of the cost function minimum that only improves with more ensemble members, and thus more cost.

The simultaneous estimation of biospheric and anthropogenic contributions to the CH₄ budget is more difficult when both emissions are in the same location. Prior information from an underlying ecosystem distribution map can be useful, as it defines the location of the biospheric sources. CH₄ emissions also depend on soil properties (Spahni et al., 2011), and therefore the distribution of wetlands and their inundation extent can be used as prior information. This approach has the advantage that emission estimates from different source categories and ecosystem types can be optimized separately by the application of different scaling factors. However, it is known that the spatial distribution of CH₄ sources relies heavily on these prior estimates, and that emissions cannot be assigned to regions outside of the predefined source regions. If the distribution in the prior or the ecosystem map is incorrect, the emission estimates would not be optimized appropriately. This approach was implemented in Tsuruta et al. (2015), and will be evaluated further in this study.

In this study, we examine emission estimates for 2000–2012 from CarbonTracker Europe-CH₄ (CTE-CH₄) with three configurations in an attempt to report a more meaningful mean and uncertainty range than those from only one simulation. CTE-CH₄ is a version of the European branch of CarbonTracker data assimilation systems (Peters et al., 2005, 2010; van der Laan-Luijkx et al., 2015). The inversions were designed to examine uncertainties related to parametrization in the system, as well as using different vertical transport schemes. The choice reflects the finding by Locatelli et al. (2013) that the regional flux estimates can differ by up to 150 % on a grid-scale depending on the transport model. On the larger scale, one important property is the interhemispheric (IH) exchange rate, which has strong effects on the

north–south gradient (Locatelli et al., 2013). The strong influence of the vertical mixing scheme was also shown by Olivé et al. (2004), which will be explicitly examined in this study. For the evaluation, simulated atmospheric CH₄ was compared with data from in situ observation sites to evaluate the statistical consistency of the CH₄ emission estimates. Furthermore, non-assimilated observations from aircraft campaigns in Europe, and ground- and satellite-based retrievals of dry air total column-averaged mole fraction (XCH₄) values from the Total Carbon Column Observing Network (TCCON) and Greenhouse gases Observing Satellite (GOSAT) were used to evaluate vertical and long-range transport. Details of the data assimilation system and its designs are described first in Sect. 2, as well as the observations used to drive and evaluate the estimates. The evaluation is discussed in Sect. 3.1, 3.2 and 3.3, followed by the range of global and regional CH₄ budget estimates (Sect. 3.4). Results are discussed in Sect. 4, comparing them to other recent estimates, and summarized in Conclusions (Sect. 5).

2 Methods and datasets

2.1 CTE-CH₄

CTE-CH₄ is an atmospheric inverse model that optimizes global surface CH₄ emissions region-wise based on an EnKF (Evensen, 2003) used to minimize a cost function:

$$J = (\mathbf{x} - \mathbf{x}^b)^T \mathbf{P}^{-1} (\mathbf{x} - \mathbf{x}^b) + (\mathbf{y} - H(\mathbf{x}))^T \mathbf{R}^{-1} (\mathbf{y} - H(\mathbf{x})), \quad (1)$$

$$\mathbf{E} = G(\mathbf{x}) \mathbf{E}^b, \quad (2)$$

where \mathbf{x} (dimension N) is a state vector that contains a set of scaling factors that multiply the CH₄ surface emissions (\mathbf{E} , dimension 360×180 , latitude \times longitude degrees) that we wish to optimize, starting from a prior estimate of these emissions (\mathbf{E}^b [360×180]) and scaling factors \mathbf{x}^b [N]. \mathbf{P} [$N \times N$] is the covariance matrix of the state vector, \mathbf{y} (dimension M) is a vector of atmospheric CH₄ observations, \mathbf{R} [$M \times M$] is a covariance matrix of the observations \mathbf{y} , and H is an observation operator [$M \times N$]. The operator G transforms the regionally estimated scaling factors \mathbf{x} to a $1^\circ \times 1^\circ$ global map, which are used to scale prior emissions \mathbf{E} . The cost function in Eq. (1) is minimized using an EnKF (Evensen, 2003) with 500 ensemble members, and the TM5 chemistry transport model (Krol et al., 2005) was used as an observation operator that transforms emissions \mathbf{E} into simulated atmospheric CH₄ ($H(\mathbf{x})$). The emissions \mathbf{E} were optimized weekly, with an assimilation window smoother length of 5 weeks.

In this study, anthropogenic and biospheric emissions were optimized, while emissions from other sources (fire, termites, and oceans) were not optimized (see Sect. 2.3). The optimal weekly mean CH₄ fluxes (F_{tot}), in region r and time (week)

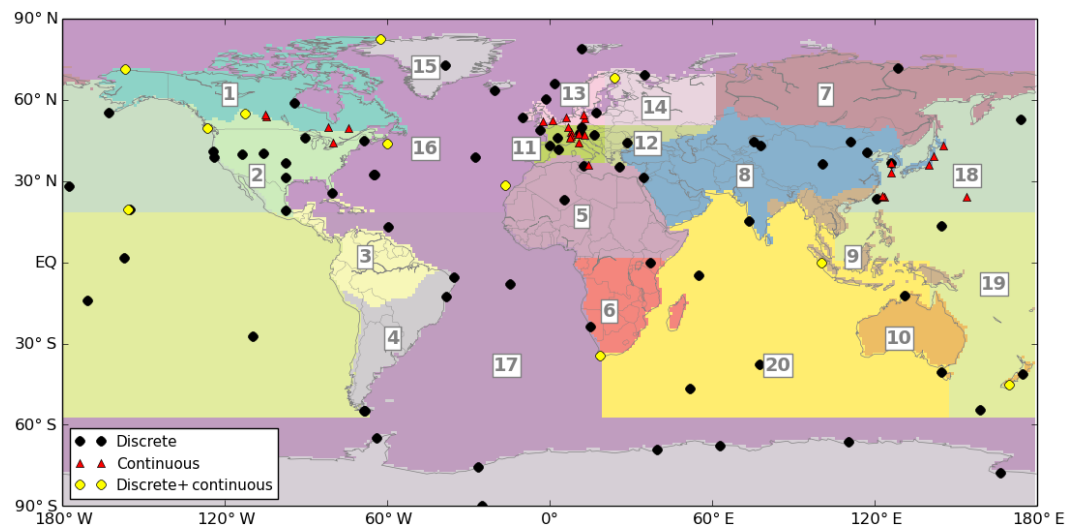


Figure 1. Modified TransCom (mTC) regions illustrated in numbers and colours and locations of sites with observations assimilated in the inversions. The names of the mTCs regions are given in Table 5.

t , were calculated as follows:

$$F_{\text{tot}}(r,t) = \lambda_{\text{bio}}(r,t) \times F_{\text{bio}}(r,t) + \lambda_{\text{anth}}(r,t) \times F_{\text{anth}}(r,t) + F_{\text{fire}}(r,t) + F_{\text{term}}(r,t) + F_{\text{oce}}(r,t), \quad (3)$$

where F_{bio} , F_{ant} , F_{fire} , F_{term} , F_{oce} , are the prior emissions from the biospheric, anthropogenic activities, fire, termites and oceans, respectively.

The optimization regional definition of CTE-CH₄ is defined based on modified TransCom (mTC) (Fig. 1) and land-ecosystem regions (Fig. S4). Land-ecosystem regions in a 1° × 1° grid were defined based on Prigent et al. (2007) and Wania et al. (2010), as in the LPJ-WHyME vegetation model (Spahni et al., 2011), and contain six land ecosystem types (LETs): inundated wetland and peatland (IWP), wet mineral soil (WMS), rice (RIC), anthropogenic land (ANT), water (WTR) and ice (ICE). Large lakes, the Mediterranean Sea, and other large bay areas were defined as WTR, similarly to Peters et al. (2007). ICE corresponds to the ice region in the mTC definition. The remainder of the land-ecosystem regions were defined according to the fraction of IWP, WMS and RIC used in LPJ-WHyME. To limit the number of degrees of freedom, only one dominant LET was assigned to each grid cell. In the following cases, the LET with the largest fraction was chosen. For grid cells where the fraction of IWP, WMS or RIC was larger than 0.1, either IWP, WMS or RIC was assigned. IWP or WMS was assigned for grid cells where the fraction of IWP or WMS were smaller than 0.1, and the prior anthropogenic emission estimates (EDGARv4.2 FT2010, see Sect. 2.3) including emissions from rice fields were zero. Furthermore, if the LPJ-WHyME biospheric emission estimates exceeded the EDGARv4.2 FT2010 emission estimates by more than 200 %, either IWP or WMS was assigned. However, if the

Table 1. List of inversion setups.

Inversion	Number of parameters and optimized sources*	TM5 convection
L ⁶² T	62, anthropogenic OR biospheric	Tiedtke (1989)
L ⁷⁸ T	78, anthropogenic AND biospheric	Tiedtke (1989)
L ⁶² G	62, anthropogenic OR biospheric	Gregory et al. (2000)

* Optimized sources per optimization region

EDGARv4.2 FT2010 emission estimates were much larger than the LPJ-WHyME biospheric emission estimates, either ANT, RIC or WTR was assigned.

In one of the two model configurations referred to as L⁶² (see also Table 1 for an overview of configurations), anthropogenic emissions were optimized in optimization regions where LETs are RIC, ANT or WTR (i.e. $\lambda_{\text{bio}}(r,t) = 0$), and biospheric emissions were optimized in optimization regions where LETs are either IWP or WMS (i.e. $\lambda_{\text{anth}}(r,t) = 0$). This mutually exclusive approach resulted in 28 biospheric regions and 34 anthropogenic optimization regions, i.e. 62 scaling factors $\lambda(t) = (\lambda_{\text{bio}}(t), \lambda_{\text{anth}}(t))$ to be optimized per week globally. This number of scaling factors was smaller than theoretically expected (20 mTCs × 5 land-ecosystem regions = 100 scaling factors) because some mTCs contain less than five ecosystem types. In the second configurations referred to as L⁷⁸, both $\lambda_{\text{bio}}(r,t)$ and $\lambda_{\text{anth}}(r,t)$ were optimized in each optimization region. In that case, the regional definition of the scaling factors for biospheric emissions was based on the combination of mTCs and land-ecosystem regions,

but oceans were treated as one region instead of five (i.e. 58 biospheric regions). The mTCs (20 regions) were used for the anthropogenic emissions. This resulted in 78 scaling factors to be optimized per week globally. Note that scaling factors were optimized based on sensitivities in the EnKF (represented in Kalman Gain matrix), and thus there is no explicitly prescribed system for choosing which of the scaling factors ($\lambda_{\text{bio}}(r, t)$ or $\lambda_{\text{anth}}(r, t)$) are adjusted more in each optimization region. A discussion of the application of land-ecosystem distribution maps and their effect on CH₄ emission inversions for a short period during summer 2007 is also included in the Supplement of this study.

For the prior uncertainty, variance of the scaling factors was set to 0.8 for all optimization regions, except for the “Ice” region (Fig. S4), which was set to 1×10^{-8} . Emissions from the “Ice” region contribute only 0.02 % of the global total emissions, and we did not expect the inversions to be able to optimize the emissions well. For L^{62} , an informative covariance matrix was used; the scaling factors for biospheric and anthropogenic emissions were assumed to be independent, and biospheric scaling factors were assumed to be correlated among mTCs based on the distance between the centres of the optimization regions (see Supplement for further details). For L^{78} , a non-informative covariance matrix was used, i.e. all optimization regions were assumed to be independent.

2.2 TM5 chemistry transport model

The atmospheric chemistry transport model TM5 (Krol et al., 2005) was used as an observation operator. TM5 was run with a $1^\circ \times 1^\circ$ (latitude \times longitude) zoom region over Europe ($24\text{--}74^\circ \text{N}$, $21^\circ \text{W--}45^\circ \text{E}$), framed by an intermediate zoom region of $2^\circ \times 3^\circ$, and a global $4^\circ \times 6^\circ$ degree resolution, driven by 3-hourly ECMWF ERA-Interim meteorological fields with 25 vertical layers. The atmospheric chemical loss, i.e. oxidation of CH₄ initiated by reaction with OH, chlorine (Cl) and an electronically excited state of oxygen ($\text{O}(^1\text{D})$), was pre-calculated based on Houweling et al. (2014) and Brühl and Crutzen (1993), and it was not adjusted in the optimization scheme. The atmospheric lifetime of CH₄ estimated from the global total annual mean atmospheric chemical loss during 2000–2012 was about 9.7 years. Interannual variability was not applied in the removal rates of the CH₄ sinks.

To establish reasonable initial conditions for the global distribution of CH₄ abundance, TM5 was run twice consecutively for 1999, starting from a uniform abundance of 1600 ppb globally using prior emission estimates. Using the final values, CTE-CH₄ was run for 2000, and the third run was used to define the initial CH₄ values at the beginning of 2000. Since atmospheric CH₄ concentrations did not increase significantly in 2000, it was assumed that this condition represents well-mixed initial atmospheric CH₄ for the experiments presented in this study.

In this study, two different convection schemes were used in TM5: Tiedtke (1989) (hereafter T1989) and Gregory et al. (2000) (hereafter G2000). The two versions differ mainly in vertical mixing in the troposphere: mixing is faster, and atmospheric CH₄ at the surface in the Northern Hemisphere (NH) is expected to be smaller with G2000 compared to T1989. Moreover, G2000 produces faster vertical mixing near the surface and also has a faster IH exchange time compared to T1989.

2.3 Prior CH₄ emissions

Five prior emission fields were used in this study and represented CH₄ release from anthropogenic, biospheric, fire, termite, and oceanic sources. Anthropogenic emissions accounted for about 60 % of total global annual CH₄ emissions during 2000–2012. For prior anthropogenic emissions, the Emissions Database for Global Atmospheric Research version 4.2 FT2010 (EDGAR v4.2 FT2010) inventory was used. The original inventory data coverage extends to 2010; for 2011–2012, emission fields were assumed to be the same as 2010. Turner et al. (2016) suggested that a large increase in anthropogenic emissions from the United States contributed significantly to the global growth in CH₄ emissions during 2002–2014. Although the 2010–2012 increase was not included in the prior, such an increase is expected to be seen in the CTE-CH₄ after optimization. A seasonal cycle was not included in the EDGAR v4.2 FT2010 estimates. Emission estimates from the biogeochemistry model LPX-Bern v1.0 (Spahni et al., 2013) were used as prior biospheric emissions, which accounted for about 30 % of prior global total emissions. Emission estimates from rice fields were excluded from the prior biospheric emissions because they were already included in the prior anthropogenic emissions. In addition, consumption of CH₄ by methanotrophic bacteria in soils was estimated by LPX-Bern, and included as surface sinks in CTE-CH₄. GFEDv3.1 (Randerson et al., 2012; van der Werf et al., 2010) was used for emission estimates from large-scale biomass burning rather than the EDGARv4.2 FT2010 inventory. GFEDv3.1 emission estimates accounted for about 3 % of prior global total emissions. The original data coverage is up to 2011, so the 2011 and 2012 emission fields were assumed to be unchanged from the last year available. However, global fire emissions in 2012 were about 2 Tg CH₄ yr^{−1} larger than in 2011, mainly due to an increase in emissions in northwest Russia during the summer (GFEDv4.1; Giglio et al., 2013). Therefore, we must be aware of an additional uncertainty in the spatial distribution of the emission sources, especially for 2012. Prior termite emissions are based on estimates from Ito and Inatomi (2012) for 2000–2006, which accounted for about 4 % of prior global total emissions. The 2006 estimate was also used for 2007–2012. The estimates by Ito and Inatomi (2012) are about 10 Tg CH₄ yr^{−1} smaller than the estimates reported by Sanderson (1996) that were used in

Bergamaschi et al. (2007), for example. Prior emission estimates from “natural” open ocean were calculated assuming a supersaturation of CH_4 in the seawater of 1.3 (Lambert and Schmidt, 1993), which accounted for about 1 % of prior global total emissions. ECMWF ERA-Interim sea surface temperature, sea ice concentration, surface pressure and wind speed (Dee et al., 2011) were used to calculate the solubility and the transfer velocity (Bates et al., 1966; Tsuruta et al., 2015). No special treatment was applied to coastal emissions of the “natural” ocean. In addition to the “natural” ocean emission estimate, an “anthropogenic” ocean emission estimate from EDGAR v4.2 FT2010 was added to the prior. Sources of anthropogenic ocean emissions are mainly from ships and other “non-road” transportation. This includes emissions around coastlines. Prior fluxes from land and ocean anthropogenic sources, and from land biospheric sources, were optimized. Fluxes from fire, termites and natural ocean sources were not optimized.

2.4 Atmospheric CH_4 observations

Atmospheric observations of CH_4 abundance (reported in units of dry-air mole fraction) collected from the World Data Centre for Greenhouse Gases (WDCGG) were assimilated in CTE- CH_4 . The set of observations consisted of discrete air samples and continuous measurements from several cooperative networks (Table 2). The observations were filtered based on observation flags provided by each contributor to avoid the influence of strong local signals on the inversions. For continuous observations, daily means from selected hours were assimilated; afternoon observations (12:00–16:00 LT) were selected for most sites, but for the high altitude sites, night-time observations (00:00–04:00 LT) were selected. These choices of sampling hours reflect a preference for well-mixed conditions that represent large source areas, and are also better captured by the TM5 transport model. Day–night selection was not applied to discrete observations. For each site, model–data mismatches (MDMs) were defined considering both the observation error and the transport model error, i.e. the ability of the transport model to simulate the observations. Note that the latter error is often much larger than the former. For the marine boundary layer (MBL) and the high latitude Southern Hemisphere (HLSH) sites, MDM was set to 4.5 ppb. For sites that capture both land and ocean signals, MDM was set to 15 ppb. For sites that capture signals from the land, MDM was set to 25 ppb. For sites with a large variation in observations due to local influences, MDM was set to 30 ppb, and for the sites that appeared problematic in the inversions, MDM was set to 75 ppb. Although the values of MDM are somewhat arbitrary, they are based on a previous study by Bruhwiler et al. (2014) and typically reflect the model forecast skill well. During assimilation, rejection thresholds were set as 3 times MDM, except for the MBL and HLSH sites. For these sites, rejection thresholds were set to 20 times MDM because assimilation

of these observations is important in the characterization of background atmospheric CH_4 . In this study, the observation covariance matrix was assumed diagonal, i.e. no temporal or spatial correlation between observations was taken into account.

2.5 Aircraft profiles for evaluation

Aircraft profiles of CH_4 abundance with altitude provide information about atmospheric CH_4 in general, but also specifically on vertical transport. Aircraft data from regular profiling that operated within the European CarboEurope project at Orléans (France), Białystok (Poland), Hegyhatsal (Hungary) and Griffin (UK) during 2006–2012, which is a part of the European Union-funded IA (Integrating Activity) project within the Integrated non- CO_2 Greenhouse gas Observation Systems (InGOS), were used for evaluation (Table 3). In addition, data from an aircraft campaign performed within the Infrastructure for Measurement of the European Carbon Cycle (IMECC) project were used. The IMECC campaign deployed a Learjet 35a with multiple vertical profiles from close to the surface up to 13 km near several TCCON sites in central Europe. For details on the airborne CH_4 measurements the reader is referred to Geibel et al. (2012). Aircraft observations were not assimilated in the inversions.

2.6 XCH_4 dataset for evaluation

In addition to the aircraft profiles and surface CH_4 measurements at in situ stations, XCH_4 from the TCCON network and the TANSO-FTS instrument on board the GOSAT spacecraft (Kuze et al., 2009) were used for evaluation. XCH_4 data provided additional information in regard to long-range transport and helped to assess the quality of the global simulations. TCCON retrievals from the GGG2014 release (Wunch et al., 2015) were used, and daily means were compared to simulated XCH_4 at each site. For GOSAT retrievals, the product reported by Yoshida et al. (2013) was used, and the regional daily mean for each mTC was compared to the corresponding simulation. The XCH_4 datasets were not assimilated in the inversions.

To facilitate a fair comparison, posterior XCH_4 were calculated using global $4^\circ \times 6^\circ \times 25$ (latitude, longitude, vertical levels) daily 3-dimensional (3-D) atmospheric CH_4 fields. For each retrieval, the global 3-D daily mean gridded atmospheric CH_4 estimates were horizontally (latitude, longitude) interpolated to the location of the retrievals to create the vertical profile of simulated CH_4 . For comparison with GOSAT and TCCON retrievals, the retrieval-specific averaging kernels (AKs) were applied to model estimates based on Rodgers and Connor (2003):

$$\hat{C} = c_a + (\mathbf{h} \circ \mathbf{a})^T (\mathbf{x} - \mathbf{x}_a), \quad (4)$$

where \hat{C} is the quantity for comparison, i.e. XCH_4 . The scalar c_a is the prior XCH_4 of each retrieval, \mathbf{h} is a ver-

Table 2. List of surface in situ observation sites used in inversions. Model–data mismatch (MDM) is used in the observation covariance matrix, and defining rejection threshold of the observations. Data type is categorized into two measurements (discrete (D) and continuous (C)).

Site Code	Station name	Country/Territory	Contributor	Latitude	Longitude	Elevation (m a.s.l.)	MDM (ppb)	Data type (D/C)	Date range* [start end] (MM/YYYY)	
ABP	Arembepe	Brazil	NOAA/ESRL	12.77° S	38.17° W	1	4.5	D	10/2006	01/2010
ALT	Alert	Canada	NOAA/ESRL	82.45° N	62.52° W	210	15.0	D	01/1999	12/2014
ALT	Alert	Canada	ECCC	82.45° N	62.52° W	210	15.0	C	01/1999	11/2012
AMS	Île Amsterdam	France	LSCE	37.8° S	77.53° E	55	4.5	D	10/2003	03/2010
AMT	Argyle	USA	NOAA/ESRL	45.03° N	68.68° W	53	30.0	D	09/2003	12/2008
AMY	Anmyeon-do	Republic of Korea	KMA	36.53° N	126.32° E	86	15.0	C	02/1999	12/2012
ARH	Arrival Heights	New Zealand	NIWA	77.80° S	166.67° E	189	4.5	D	01/1999	11/2014
ASC	Ascension Island	St. Helena, Ascension und Tristan da Cunha	NOAA/ESRL	7.92° S	14.42° W	54	4.5	D	01/1999	12/2014
ASK	Assekrem	Algeria	NOAA/ESRL	23.18° N	5.42° E	2728	25.0	D	01/1999	12/2014
AZR	Terceira Island	Portugal	NOAA/ESRL	38.77° N	27.38° W	40	15.0	D	01/1999	12/2014
BAL	Baltic Sea	Poland	NOAA/ESRL	55.35° N	17.22° E	28	75.0	D	01/1999	06/2011
BGU	Begur	Spain	LSCE	41.83° N	3.33° E	30	15.0	D	04/2000	10/2010
BHD	Baring Head	New Zealand	NOAA/ESRL	41.41° S	174.87° E	80	4.5	D	10/1999	12/2014
BKT	Bukit Koto Tabang	Indonesia	NOAA/ESRL	0.20° S	100.32° E	865	75.0	D	01/2004	11/2014
BKT	Bukit Koto Tabang	Indonesia	BMG_EMPA	0.20° S	100.32° E	896.5	75.0	C	10/2009	12/2013
BME	St. David's Head	UK	NOAA/ESRL	32.37° N	64.65° W	30	15.0	D	01/1999	01/2010
BMW	Tudor Hill	UK	NOAA/ESRL	32.27° N	64.88° W	30	15.0	D	01/1999	12/2014
BRW	Barrow	USA	NOAA/ESRL	71.32° N	156.60° W	11	15.0	C	01/1999	12/2011
BRW	Barrow	USA	NOAA/ESRL	71.32° N	156.60° W	11	15.0	D	01/1999	12/2014
BSC	Black Sea	Romania	NOAA/ESRL	44.17° N	28.68° E	3	75.0	D	01/1999	12/2011
CBA	Cold Bay	USA	NOAA/ESRL	55.20° N	162.72° W	25	15.0	D	01/1999	12/2014
CDL	Candle Lake	Canada	ECCC	53.87° N	104.65° W	630	25.0	C	06/2002	12/2007
CGO	Cape Grim	Australia	NOAA/ESRL	40.68° S	144.68° E	94	4.5	D	01/1999	12/2014
CHL	Churchill	Canada	ECCC	58.75° N	94.07° W	76	15.0	D	04/2007	12/2013
CHM	Chibougama	Canada	ECCC	49.68° N	74.34° W	393	15.0	C	08/2007	12/2010
CHR	Christmas Island	Kiribati	NOAA/ESRL	1.70° N	157.17° W	3	4.5	D	01/1999	10/2014
CMN	Monte Cimone	Italy	UNIURB/ISAC	44.18° N	10.70° E	2172	15.0	C	07/2008	12/2011
COI	Cape Ochiishi	Japan	NIES	43.15° N	145.50° E	100	4.5	C	01/1999	12/2010
CPT	Cape Point	Southern Africa	NOAA/ESRL	34.35° S	18.49° E	230	25.0	D	02/2010	12/2014
CPT	Cape Point	Southern Africa	SAWS	34.35° S	18.49° E	260	15.0	C	01/1999	12/2013
CRI	Cape Rama	India	CSIRO	15.08° N	73.83° E	60	75.0	D	01/1999	01/2013
CRZ	Crozet	France	NOAA/ESRL	46.45° S	51.85° E	120	4.5	D	01/1999	11/2014
CYA	Casey Station	Australia	CSIRO	66.28° S	110.52° E	2	4.5	D	01/1999	10/2014
DEU	Deuselbach	Germany	UBA	49.77° N	7.05° E	480	15.0	C	01/1999	07/2004
EGB	Egbert	Canada	ECCC	44.23° N	79.78° W	226	75.0	C	03/2005	12/2012
EIC	Easter Island	Chile	NOAA/ESRL	27.15° S	109.45° W	50	4.5	D	01/1999	12/2014
ESP	Estevan Point	Canada	CSIRO	49.38° N	126.55° W	39	25.0	D	01/1999	01/2002
ESP	Estevan Point	Canada	ECCC	49.38° N	126.55° W	39	25.0	C	03/2009	12/2012
ETL	East Trout Lake	Canada	ECCC	54.35° N	104.98° W	492	25.0	C	08/2005	12/2012
FIK	Finokalia	Greece	LSCE	35.34° N	25.67° E	150	15.0	D	05/1999	11/2010
FSD	Fraserdale	Canada	ECCC	49.88° N	81.57° W	210	15.0	C	01/1999	12/2012
GLH	Giordan	Malta	UMLT	36.07° N	14.22° E	167	15.0	C	10/2012	12/2012
	Lighthouse									
GMI	Guam	US Territory	NOAA/ESRL	13.43° N	144.78° E	2	15.0	D	01/1999	12/2014
GPA	Gunn Point	Australia	CSIRO	12.25° S	131.05° E	37	75.0	D	08/2010	10/2014
GSN	Gosan	Republic of Korea	GERC	33.15° N	126.12° E	144	15.0	C	02/2002	05/2011
HAT	Hateruma	Japan	NIES	24.05° N	123.80° E	47	15.0	C	01/1999	12/2010
HBA	Halley Bay	UK	NOAA/ESRL	75.58° S	26.50° W	30	4.5	D	01/1999	11/2014
HPB	Hohenpeißenberg	Germany	NOAA/ESRL	47.80° N	11.01° E	985	25.0	D	04/2006	12/2014
HUN	Hegyatsal	Hungary	NOAA/ESRL	46.95° N	16.65° E	344	75.0	D	01/1999	12/2014
ICE	Heimaey	Iceland	NOAA/ESRL	63.34° N	20.29° W	118	15.0	D	01/1999	12/2014
IZO	Izaña (Tenerife)	Spain	NOAA/ESRL	28.30° N	16.48° W	2360	15.0	D	01/1999	12/2014
IZO	Izaña (Tenerife)	Spain	AEMET	28.30° N	16.48° W	2360	15.0	C	01/1999	12/2013
JFJ	Jungfrau	Switzerland	EMPA	46.55° N	7.99° E	3583	15.0	C	02/2005	12/2012
KEY	Key Biscayne	USA	NOAA/ESRL	25.67° N	80.20° W	3	25.0	D	01/1999	12/2014
KMW	Kollumerwaard	Netherlands	RIVM	53.33° N	6.28° E	0	15.0	C	01/1999	12/2010
KUM	Cape Kumukahi	USA	NOAA/ESRL	19.52° N	154.82° W	3	4.5	D	01/1999	12/2014
KZD	Sary Taukum	Kazakhstan	NOAA/ESRL	44.45° N	75.57° E	412	75.0	D	01/1999	08/2009
KZM	Plateau Assy	Kazakhstan	NOAA/ESRL	43.25° N	77.88° E	2519	25.0	D	01/1999	08/2009

Table 2. Continued.

Site Code	Station name	Country/Territory	Contributor	Latitude	Longitude	Elevation (m a.s.l.)	MDM (ppb)	Data type (D/C)	Date range* [start end] (MM/YYYY)	
LAU	Lauder	New Zealand	NIWA	45.03° S	169.67° E	370	15.0	C	01/2007	12/2013
LAU	Lauder	New Zealand	NIWA	45.03° S	169.67° E	370	15.0	D	02/2010	11/2014
LEF	Park Falls	USA	NOAA/ESRL	45.93° N	90.27° W	868	30.0	D	01/1999	12/2014
LLB	Lac La Biche	Canada	NOAA/ESRL	54.95° N	112.45° W	540	75.0	D	01/2008	02/2013
LLB	Lac La Biche (Alberta)	Canada	ECCC	54.95° N	112.45° W	540	75.0	C	04/2007	12/2012
LLN	Lülin	Taiwan	NOAA/ESRL	23.47° N	120.87° E	2862	25.0	D	08/2006	12/2014
LMP	Lampedusa	Italy	NOAA/ESRL	35.52° N	12.62° E	45	25.0	D	10/2006	12/2014
LPO	Île Grande	France	LSCE	48.80° N	3.58° W	20	15.0	D	11/2004	03/2010
MAA	Mawson	Australia	CSIRO	67.62° S	62.87° E	32	4.5	D	01/1999	12/2014
MEX	High Altitude Global Climate Observation Center	Mexico	NOAA/ESRL	18.98° N	97.31° W	4464	15.0	D	01/2009	11/2014
MHD	Mace Head	Ireland	NOAA/ESRL	53.33° N	9.90° W	25	25.0	D	01/1999	12/2014
MID	Sand Island	US Territory	NOAA/ESRL	28.21° N	177.38° W	4	15.0	D	01/1999	12/2014
MKN	Mt. Kenya	Kenya	NOAA/ESRL	0.05° S	37.30° E	3897	25.0	D	12/2003	06/2011
MLO	Mauna Loa	USA	NOAA/ESRL	19.53° N	155.58° W	3397	15.0	C	01/1999	12/2011
MLO	Mauna Loa	USA	NOAA/ESRL	19.53° N	155.58° W	3397	15.0	D	01/1999	12/2014
MNM	Minamitorishima	Japan	JMA	24.30° N	153.97° E	8	15.0	C	01/1999	01/2014
MQA	Macquarie Island	Australia	CSIRO	54.48° S	158.97° E	12	4.5	D	01/1999	12/2014
NAT	Natal	Brazil	NOAA/ESRL	5.51° S	35.26° W	15	15.0	D	09/2010	12/2014
NGL	Neuglobsow	Germany	UBA	53.17° N	13.03° E	68.4	15.0	C	01/1999	12/2013
NMB	Gobabeb	Namibia	NOAA/ESRL	23.58° S	15.03° E	456	25.0	D	01/1999	12/2014
NWR	Niwot Ridge (T-van)	USA	NOAA/ESRL	40.05° N	105.58° W	3523	15.0	D	01/1999	12/2014
OXK	Ochsenkopf	Germany	NOAA/ESRL	50.03° N	11.80° E	1009	75.0	D	03/2003	12/2014
PAL	Pallas-Sammaltunturi	Finland	NOAA/ESRL	67.97° N	24.12° E	560	15.0	D	12/2001	12/2014
PAL	Pallas-Sammaltunturi	Finland	FMI	67.58° N	24.06° E	572	15.0	C	02/2004	12/2013
PDM	Pic du Midi	France	LSCE	42.93° N	0.13° E	2877	15.0	D	06/2001	08/2010
PRS	Plateau Rosa	Italy	RSE	45.93° N	7.70° E	3490	15.0	C	01/2005	12/2013
PSA	Palmer Station	USA	NOAA/ESRL	64.92° S	64.00° W	10	4.5	D	01/1999	12/2014
PTA	Point Arena	USA	NOAA/ESRL	38.95° N	123.73° W	17	25.0	D	01/1999	05/2011
PUY	Puy de Dôme	France	LSCE	45.77° N	2.97° E	1465	15.0	D	07/2001	11/2010
RGL	Ridge Hill	UK	UNIVBRIS	52.00° N	2.54° W	294	25.0	C	03/2012	11/2012
RPB	Ragged Point	Barbados	NOAA/ESRL	13.17° N	59.43° W	45	15.0	D	01/1999	12/2014
RYO	Ryōri	Japan	JMA	39.03° N	141.83° E	260	15.0	C	01/1999	01/2014
SDZ	Shangdianzi	China	CMA_NOAA/ESRL	40.65° N	117.11° E	293	15.0	D	09/2009	12/2014
SEY	Mahe Island	Seychelles	NOAA/ESRL	4.67° S	55.17° E	3	4.5	D	01/1999	12/2014
SGP	Southern Great Plains	USA	NOAA/ESRL	36.60° N	97.49° W	314	75.0	D	04/2002	12/2014
SHM	Shemya Island	USA	NOAA/ESRL	52.72° N	174.10° E	40	25.0	D	01/1999	12/2014
SIS	Shetland	UK	CSIRO	60.17° N	1.17° W	30	15.0	D	01/1999	12/2003
SMO	Tutuila (Cape Matatula)	US Territory	NOAA/ESRL	14.24° S	170.57° W	42	4.5	D	01/1999	12/2014
SNB	Sonnblick	Austria	EAA	47.05° N	12.95° E	3111	15.0	C	04/2012	12/2013
SPO	South Pole	USA	NOAA/ESRL	89.98° S	24.80° W	2810	4.5	D	01/1999	12/2014
SSL	Schauinsland	Germany	UBA	47.92° N	7.92° E	1205	15.0	C	12/1998	12/2013
STM	Ocean Station “M”	Norway	NOAA/ESRL	66.00° N	2.00° E	5	15.0	D	01/1999	11/2009
SUM	Summit	Denmark	NOAA/ESRL	72.58° N	38.48° W	3238	15.0	D	08/2000	12/2014
SYO	Syowa Station	Japan	NOAA/ESRL	69.00° S	39.58° E	11	4.5	D	01/1999	12/2014
TAC	Tacolneston Tall Tower	UK	UNIVBRIS	52.52° N	1.14° E	156	25.0	C	07/2012	11/2012
TAP	Tae-ahn Peninsula	Republic of Korea	NOAA/ESRL	36.73° N	126.13° E	20	75.0	D	01/1999	12/2014
TER	Teriberka	Russian Federation	MGO	69.20° N	35.10° E	42	15.0	D	01/1999	12/2014
THD	Trinidad Head	USA	NOAA/ESRL	41.05° N	124.15° W	107	25.0	D	04/2002	12/2014
TIK	Tiksi	Russian Federation	NOAA/ESRL	71.59° N	128.89° E	31	15.0	D	08/2011	12/2014
TKB	Tsukuba	Japan	MRI	36.05° N	140.13° E	26	15.0	C	01/1999	06/2002
USH	Ushuaia	Argentina	NOAA/ESRL	54.85° S	68.31° W	12	4.5	D	01/1999	12/2014
UTA	Wendover	USA	NOAA/ESRL	39.90° N	113.72° W	1320	25.0	D	01/1999	12/2014
UUM	Ulaan-Uul	Mongolia	NOAA/ESRL	44.45° N	111.10° E	914	25.0	D	01/1999	12/2014

Table 2. Continued.

Site Code	Station name	Country/Territory	Contributor	Latitude	Longitude	Elevation (m a.s.l.)	MDM (ppb)	Data type (D/C)	Date range* [start end] (MM/YYYY)	
WIS	Sedé Boqer	Israel	NOAA/ESRL	31.13° N	34.88° E	400	25.0	D	01/1999	12/2014
WKT	Moody	USA	NOAA/ESRL	31.31° N	97.33° W	251	30.0	D	02/2001	10/2010
WLG	Mt. Waliguan	China	CMA_NOAA	36.28° N	100.90° E	3810	15.0	D	01/1999	12/2014
WSA	Sable Island	Canada	ECCC	43.93° N	60.02° W	5	25.0	C	06/2003	12/2012
WSA	Sable Island	Canada	ECCC	43.93° N	60.02° W	5	25.0	D	11/1999	12/2013
YON	Yonagunijima	Japan	JMA	24.47° N	123.02° E	30	15.0	C	02/1999	01/2014
ZEP	Zeppelinfjellet (Ny-Alesund)	Norway	NOAA/ESRL	78.90° N	11.88° E	475	15.0	D	01/1999	12/2014
ZGT	Zingst	Germany	UBA	54.43° N	12.73° E	1	15.0	C	01/1999	01/2003
ZSF	Zugspitze/Schneefernerhaus	Germany	UBA	47.42° N	10.98° E	2673.5	15.0	C	12/2001	12/2011
ZUG	Zugspitze	Germany	UBA	47.42° N	10.98° E	2965.5	15.0	C	12/1998	12/2001

* Date range is only presented since January 1999 until December 2014. Note that some sites have longer records.

Table 3. List of aircraft profile measurement sites.

Site Code	Station Name	Country	Project	Sampling heights (m)		Data range (year)	Prior RMSE (ppb)			Posterior RMSE (ppb)		
				[min.]	[max.]		L ⁶² T	L ⁷⁸ T	L ⁶² G	L ⁶² T	L ⁷⁸ T	L ⁶² G
ORL	Orléans	France	CarboEurope	100.0	3200	2006–2012	101.2	101.2	88.0	39.2	37.4	40.8
BIK	Bialystok	Poland	CarboEurope	223.8	3026	2007–2011	82.1	82.1	68.6	24.4	27.2	26.1
HNG	Hegyatsal	Hungary	CarboEurope	300.0	3250	2006–2009	81.5	81.5	66.4	25.3	25.2	27.5
GRI	Griffin	UK	CarboEurope	550.0	3100	2006–2010	74.7	74.7	59.9	12.9	12.9	11.0
IMECC*			IMECC	19.5	13240	2009	79.1	79.1	81.6	17.4	19.1	17.6

* Observations from the IMECC campaign contain samples from several sites and routes, i.e. the location is not site specific. Posterior with smallest RMSE is marked in bold.

tical summation vector, α is an absorber-weighted AKs of each retrieval, \mathbf{x} is a model profile, and \mathbf{x}_a is the prior profile of the retrieval. For the TCCON retrievals, one prior profile was provided each day, which was scaled to get the observed profiles that optimize the spectral fit (Wunch et al., 2011). Prior profiles of GOSAT retrievals were provided for each retrieval (Yoshida et al., 2013). Model-estimated XCH₄ values were calculated for each site for the comparison with TCCON XCH₄, while the spatial mean of XCH₄ for each mTC was used for comparison with the GOSAT retrievals.

2.7 Inversion setups

In this study, three inversions were performed, which differed in number of parameters and TM5 convection schemes: (L⁶²T) using L⁶² configuration with the T1989 convection scheme, (L⁷⁸T) using L⁷⁸ configuration with the T1989 convection scheme, and (L⁶²G) using L⁶² configuration with the G2000 convection scheme (Table 1). Prior and posterior CH₄ abundance was estimated with TM5 using prior and posterior emission estimates, respectively. Posterior CH₄ was also estimated using the respective convection schemes in the forward runs.

3 Results

Before presenting and discussing the estimated CH₄ surface fluxes, agreements with the observations used in the assimilation (Sect. 3.1), and with independent measurements from aircraft (Sect. 3.2) and remote sensing products (Sect. 3.3), are demonstrated.

3.1 Atmospheric CH₄

Atmospheric CH₄ values simulated using prior fluxes (prior atmospheric CH₄) increase continuously during 2000–2012, and quickly exceed observed atmospheric CH₄ levels, especially in the NH (Figs. 2, 3). The seasonal cycle of prior atmospheric CH₄ values agrees poorly with the observations, with a positive bias from winter to summer in the NH and around the end of each year in the Southern Hemisphere (SH) (Fig. 2). Furthermore, prior atmospheric CH₄ values are negatively biased compared to the observations in the SH during 2002–2004 (Fig. 2). This is likely due to an underestimation in the prior emissions in the SH. Posterior atmospheric CH₄ values generally match the observations to a level close to the expected model–data mismatch, indicating a proper choice of observation covariance. A seasonal bias remains in the NH (especially in L⁶²T), and the decrease in atmospheric CH₄ in the SH around 2002–2004 also remains in the posterior, although shorter in duration and of smaller magnitude

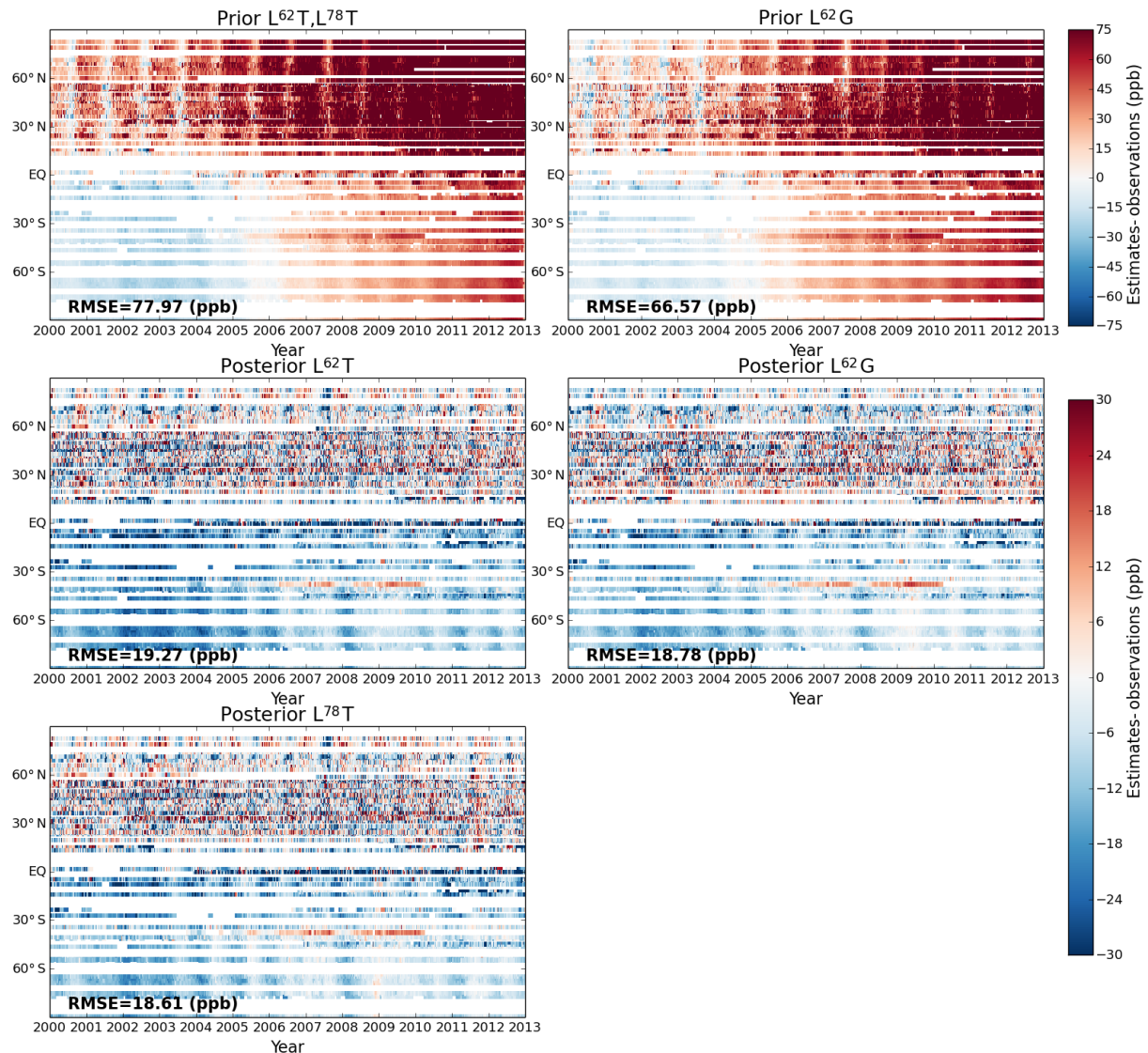


Figure 2. Differences in CH₄ (ppb) between the assimilated observations and model estimates.

than in the prior (Fig. 2). The negative bias in posterior atmospheric CH₄ around the equator remains unresolved throughout the study period in all inversions, and mainly originates from the sites Bukit Koto Tabang, Indonesia (BKT), (−25 to −27 ppb), and Mt. Kenya, Kenya (MKN) (−18 to −23 ppb). The posterior atmospheric CH₄ values are especially low relative to observations during June–October. The bias became smaller when CH₄ emissions were increased in the South American tropical mTC region, although this led to compensating fluxes and mismatches with observations elsewhere (not shown). Posterior emissions for the South American tropical region (mTC3) remain similar to the prior, and the inversion does not significantly decrease the uncertainty of the prior emission estimates in this mTC (see Sect. 3.4.4 and 4.2).

Agreement between simulated CH₄ and surface observations is slightly better in L⁷⁸T and L⁶²G than in L⁶²T (Fig. 2), as indicated by the root mean square error (RMSE), which is about 0.5 ppb smaller. In addition, the biases in annual amplitude are about 1–2 ppb smaller. The negative bias in the SH from 2002 to 2004 is seen in all inversions, but is most prominent in L⁶²T. Although the difference in the average RMSE is small, it is significant as it is calculated from all the observations assimilated in the study period. In addition, differences are significant when the ensemble distributions of posterior atmospheric CH₄ are considered. The spread (1 standard deviation (SD)) of ensembles is less than 5 ppb for most sites and less than 1 ppb for MBL sites, mostly located in the SH.

Further evidence of poorer performance in L⁶²T than in other runs is seen in its global fluxes. L⁶²T produced the smallest total global emission estimates for 2002–2004,

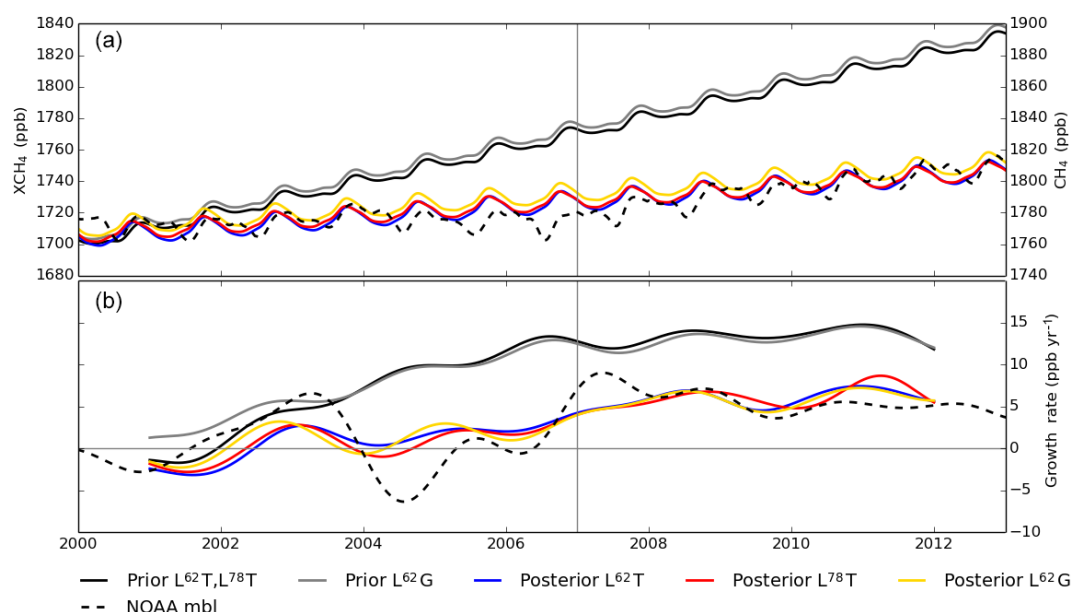


Figure 3. Top: simulated posterior and prior global mean XCH_4 (left-hand y axis), and NOAA globally averaged surface CH_4 (right-hand y axis). Bottom: growth rates of simulated XCH_4 , and of observed CH_4 . The growth rates were calculated using the methods in Thoning et al. (1989). Vertical and horizontal lines indicate 2007 and zero GR to guide the eye, respectively.

which in turn led to the largest increase in the total global emission estimates from 2001–2006 to 2007–2012. Based on previous studies (e.g. Bergamaschi et al., 2013; Bousquet et al., 2006; Bruhwiler et al., 2014; Fraser et al., 2013), the increases in L^{78}T and L^{62}G are more reasonable (see Sect. 3.4.1). The differences in RMSE and bias between the latter inversion estimates are small near 30°N , where many observations are located. However, the RMSE and bias in L^{78}T are about 1 and 2 ppb smaller at high northern latitudes ($60\text{--}75^\circ\text{N}$), and about 3 and 6 ppb larger around the equator ($\text{EQ}\text{--}15^\circ\text{N}$) than in L^{62}G , respectively. Moreover, low atmospheric CH_4 values in the SH during 2002–2004 are not as prominent in the prior when the G2000 convection scheme is used (Fig. 2), probably due to enhanced transport between the NH and SH in L^{62}G . Mean Chi-squared statistics (Michalak et al., 2005) of the observations are typically between 0 and 2, and follow normal distributions (not shown), which again indicates that the MDM estimates are appropriate at most of the sites.

In contrast to the prior, the growth rate (GR) of posterior XCH_4 does not change strongly before 2007, but increases after 2007 (Fig. 3). All inversions show an increase in XCH_4 by about 6 ppb yr^{-1} after 2007, with some seasonal and inter-annual variations (Fig. 3). The timing of the change in posterior XCH_4 GR is in line with the GR calculated from the global network of NOAA MBL observations (Dlugokencky et al., 2011) and with the retrieved XCH_4 GR at Park Falls (Fig. 3). This indicates that the GR of prior XCH_4 is too large throughout 2000–2012 (see also Fig. 2), and this can only result from overestimated emissions or underestimated loss of

CH_4 . Note that the NOAA MBL observations compared in Fig. 3 are calculated from surface observations.

3.2 Evaluation with aircraft measurements

Posterior atmospheric CH_4 generally agrees well with independent vertical profiles from aircraft. The average RMSE decreased from 80 ppb in the prior to 24 ppb in the posterior (Fig. 4, Table 3). The RMSE between posterior and observed atmospheric CH_4 values is smallest for Griffing, UK (GRI) (< 12.9 ppb), and largest for Orléans, France (ORL) (> 37.4 ppb) (Fig. 4). The model performance at in situ sites near GRI is good, i.e. the correlations between assimilated observations and posteriors are high, and the RMSE is equal to or smaller than the MDM (Fig. 5). This suggests that emission estimates are well constrained, at least in the NH, although the RMSE is much larger than those at surface sites due to vertical transport. The model performance at in situ sites near ORL is poor, and the bias in the ORL profiles extends up to 2 km, which was also seen in Bergamaschi et al. (2015). The comparison with IMECC observations from central Europe shows the effect of the convection scheme on the profiles above 2 km. Negative biases are seen in the inversion estimates using the T1989 scheme at 2–10 km. The bias in the inversion estimates using the G2000 scheme is small at around 2–10 km, but is positive in the upper troposphere and lower stratosphere, where the estimates using T1989 better match the observations. This could however be due to diffusive transport near the tropopause simulated by the 25 vertical layers in TM5. The use of a higher vertical resolution

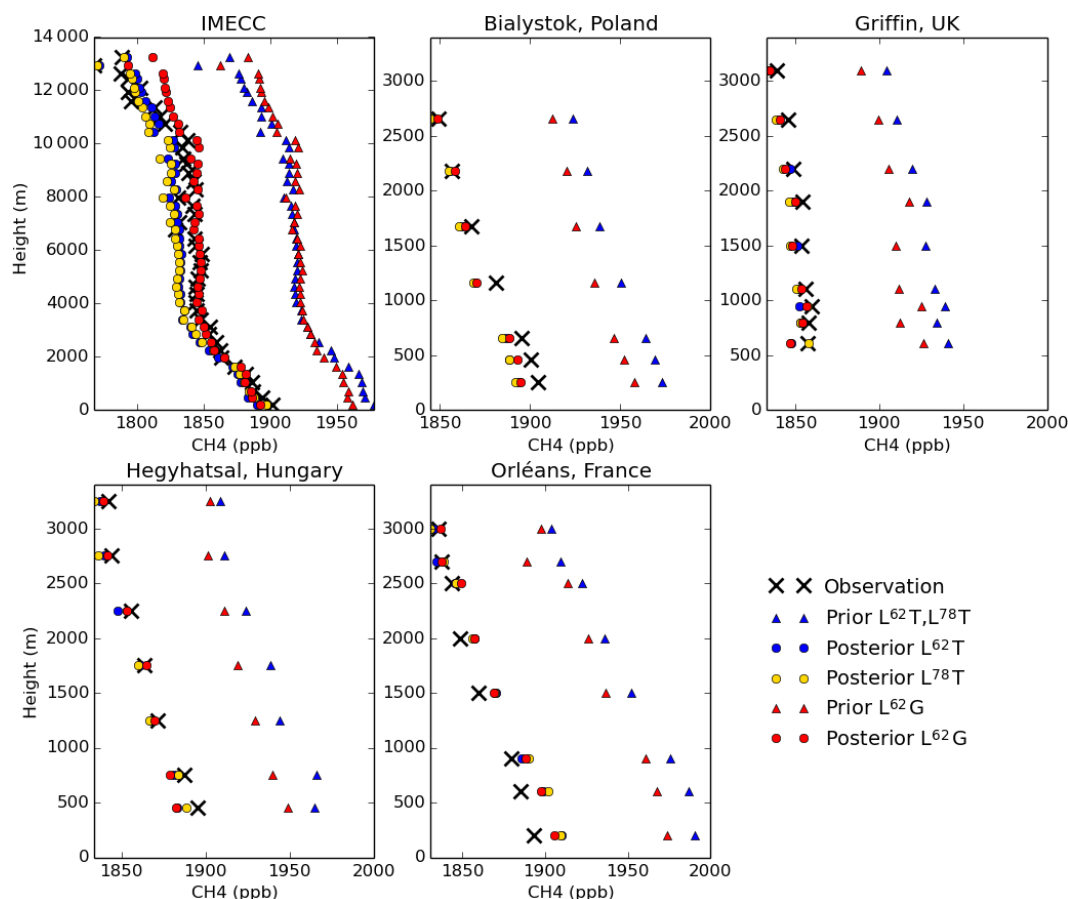


Figure 4. Vertical profiles of atmospheric CH₄ (ppb) from aircraft and posterior estimates. For each site, the medians were calculated and plotted for both observations and posterior estimates for each altitude band.

of TM5 might improve the agreement with observations at higher altitudes for both convection schemes.

3.3 Evaluation with TCCON and GOSAT XCH₄

XCH₄ provides additional information about the spatial distribution of atmospheric CH₄. TCCON and GOSAT XCH₄ retrievals were not assimilated in the inversions, so the following comparisons also allow an assessment of model performance at independent locations and times.

For many TCCON sites in the NH, the XCH₄ in L⁶²T and L⁷⁸T is slightly lower than observed, but the trend and seasonal variability are generally well captured. However, the 2007–2012 trends at Izaña (Spain), Park Falls (USA) and Lamont (USA) are much stronger than in the retrievals (Fig. 6). Since the emission estimates at similar latitudes would affect the XCH₄ estimates, this could be an effect of the strongly increasing northern temperate emission estimates after 2007 (Sect. 3.4.2). The RMSE between the estimates and retrievals is smallest in L⁶²G at all sites, except at Garmisch, Germany (Table 4). Garmisch is a mountain site (altitude 734 m a.s.l.), and the mean of observed XCH₄ is statistically significantly

lower than at nearby sites, e.g. Karlsruhe, Germany, and Bialystok, Poland (Figs. 6, S5).

For the SH TCCON sites, a strong negative bias is found in all inversions (Figs. 6, S5). Agreement is especially poor for Wollongong, which has the largest RMSE (more than 30 ppb) among all TCCON sites in all inversions (Table 4). As the site is located in the city of Wollongong, where the influence of local emissions is high, it is difficult for models to reproduce XCH₄ well (Fraser et al., 2013). The comparison with the nearest in situ site, Cape Grim, Australia (CGO) shows that the negative bias is much smaller (−6 to −11 ppb) compared to Wollongong (−32 to −35 ppb), and the correlation with the retrievals is high (> 0.85). In addition, the negative bias in XCH₄ is much smaller (−12 to −15 ppb) at background site Lauder, New Zealand (LAU) and the correlation at the LAU in situ site is again strong (> 0.85) in all inversions. The disagreement at Darwin is probably due to little constraint of the emissions. Although in situ observations at Gunn Point, Australia (GPA) were assimilated, the inversion probably did not benefit significantly from these observations because data were available only after mid-2010, and the MDM was set high (75 ppb). Furthermore, emissions from

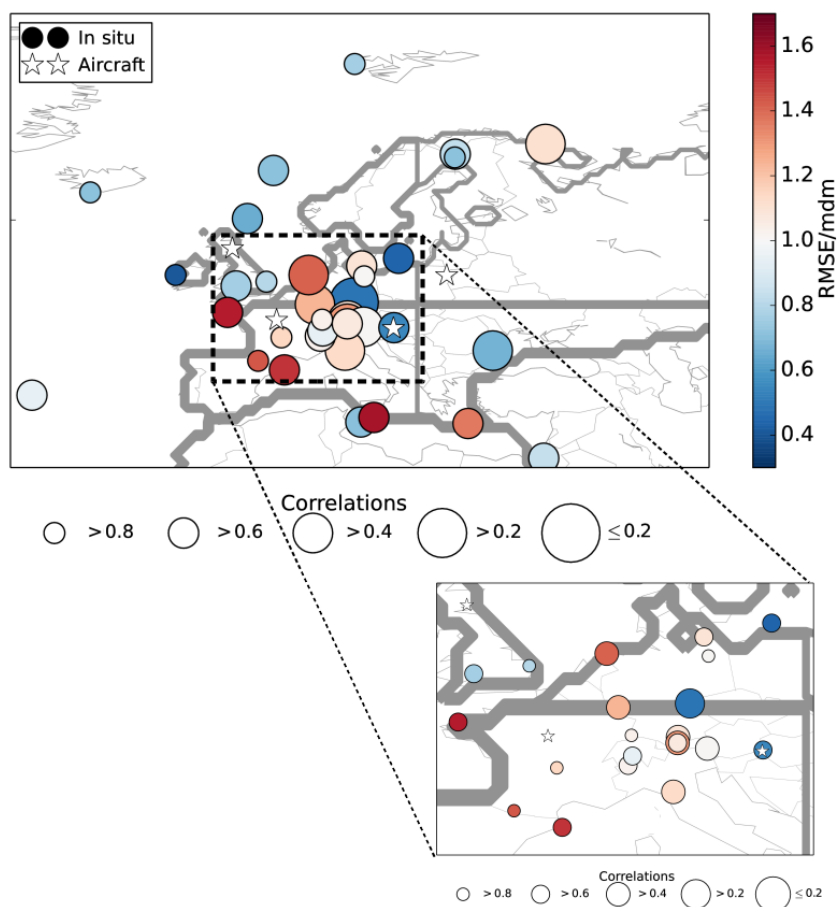


Figure 5. Performance of inversion $L^{62}G$ at European in situ observation sites, whose data were assimilated in the model, and at the locations of four aircraft campaigns. The campaign locations are marked with stars. Aircraft observations were used for evaluation. The colour of the marker for the in situ observation site is determined by the RMSE of observed and simulated posterior atmospheric CH_4 values divided by the pre-defined MDM. The radius of each circle provides the correlation between observed and simulated posterior atmospheric CH_4 values, where a larger radius corresponds to weaker correlation. Thick grey lines identify the mTC borders.

the tropics also affect the XCH_4 estimates in Australia. Our emission estimates for the tropics ($30^\circ S$ – $30^\circ N$) are about 10 – $20 \text{ Tg } CH_4 \text{ yr}^{-1}$ smaller than the estimates by Houweling et al. (2014), for example. When the prior emission estimates for the South American tropical region (mostly between $15^\circ S$ – $15^\circ N$) were increased (see Sect. 3.1), agreement in the SH improved (not shown). The comparison with GOSAT XCH_4 also supports the finding from the comparison with the TCCON retrievals, showing a mean negative bias of 13 ppb in the SH (Fig. S6). We currently do not have sufficient information to correct the errors that affected the SH XCH_4 in our system, or to identify the exact cause.

Spring peaks seen in GOSAT XCH_4 in global, ocean and the Asian tropical mTC region point to an important role of the vertical mixing scheme, which are well captured in $L^{62}G$, but not in $L^{62}T$ and $L^{78}T$ (Figs. 7, S6). The difference is statistically significant considering the ensemble distribution. Monthly emission estimates in $L^{62}G$ are generally larger than in $L^{62}T$ and $L^{78}T$ during November–April, espe-

cially in the northern-latitude temperate regions (35 – $60^\circ N$, Fig. S7). This suggests that winter emissions in the northern latitude temperate regions, enhanced in the model by faster vertical mixing around the surface, play an important role to reproduce the XCH_4 seasonal cycle in the tropics well.

Although GOSAT retrievals are valuable for evaluating model performance, it is important to keep in mind that the satellite retrievals do not always agree with ground-based TCCON retrievals. GOSAT XCH_4 has been evaluated against TCCON retrievals, but biases in the GOSAT products remain, especially in the latitudinal gradient (Yoshida et al., 2013). This is probably one of the reasons for the positive model bias in the NH compared to GOSAT (Fig. S6). Furthermore, the seasonal amplitude of GOSAT XCH_4 is much smaller than that of the posterior estimates, especially in the SH (Fig. S6). This is not in line with the TCCON comparison (Figs. 6, S5), which suggests that disagreement with GOSAT XCH_4 in the latitudinal gradient and the seasonal amplitude may not only be due to problems in the inversions.

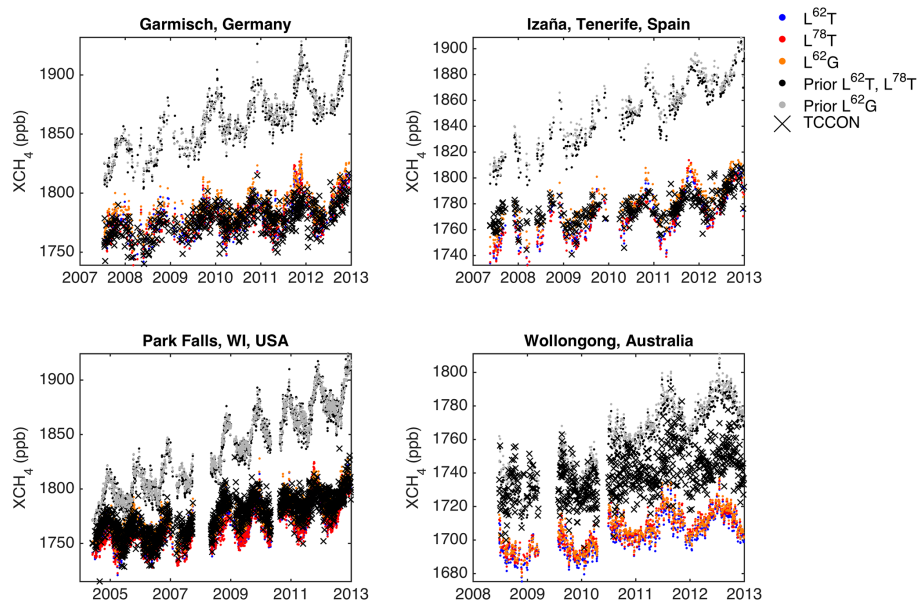


Figure 6. Observed and simulated daily mean XCH₄ at TCCON sites.

Table 4. Root mean square error (RMSE) between TCCON and model XCH₄ with averaging kernel applied (ppb). The inversion with the smallest posterior RMSE is marked in bold.

Site names	Coordinates		Prior		Posterior		
	Latitude	Longitude	L ⁶² T, L ⁷⁸ T	L ⁶² G	L ⁶² T	L ⁷⁸ T	L ⁶² G
Eureka, Canada	80.05° N	86.42° W	80.2	78.6	13.6	13.9	8.8
Sodankylä, Finland	67.37° N	26.63° E	85.1	82.5	13.3	13.2	11.3
Bialystok, Poland	53.23° N	23.03° E	75.5	75.6	17.2	17.4	10.4
Karlsruhe, Germany	49.10° N	8.44° E	86.4	87.8	12.7	13.4	11.2
Garmisch, Germany	47.48° N	11.06° E	86.8	88.1	11.7	12.1	15.3
Park Falls, WI, USA	45.95° N	90.27° W	65.5	66.9	13.9	15.7	10.6
Indianapolis, IN, USA	39.86° N	86.00° W	83.5	85.1	11.9	13.6	8.7
Lamont, OK, USA	36.60° N	97.49° W	69.5	73.3	17.0	19.6	12.4
Pasadena, CA, USA (Caltech ¹)	34.14° N	118.13° W	78.6	88.2	14.3	16.6	11.0
Pasadena, CA, USA (JPL ²)	34.12° N	118.18° W	41.5	45.9	26.6	27.9	17.9
Pasadena, CA, USA (JPL ³)	34.12° N	118.18° W	75.3	80.1	24.1	25.4	16.3
Saga, Japan	33.24° N	130.29° E	80.1	85.6	26.2	26.8	18.6
Izaña, Tenerife, Spain	28.30° N	16.50° W	74.8	80.8	11.9	12.8	10.0
Ascension Island	7.92° S	14.33° W	51.5	57.0	26.8	26.2	21.7
Darwin, Australia	12.42° S	130.89° E	29.1	32.5	28.3	26.9	25.4
Réunion, France	20.90° S	55.49° E	44.5	48.3	27.1	25.5	24.7
Wollongong, Australia	34.41° S	150.88° E	25.0	29.4	36.6	34.4	34.0
Lauder, New Zealand (120HR)	45.04° S	169.68° E	17.9	22.6	23.6	21.4	20.2
Lauder, New Zealand (125HR)	45.04° S	169.68° E	38.8	44.6	23.4	21.2	20.7

¹ California Institute of Technology, 2012. ² Jet Propulsion Laboratory, 2007–2008. ³ Jet Propulsion Laboratory, 2011–2012.

Table 5. Root mean square error (RMSE) between GOSAT and model XCH₄ with averaging kernel applied (ppb). The inversions with the smallest RMSE are marked in bold.

Region (mTC)	Prior		Posterior		
	L ⁶² T, L ⁷⁸ T	L ⁶² G	L ⁶² T	L ⁷⁸ T	L ⁶² G
Global (1–20)	68.5	68.5	9.5	9.7	5.1
Europe (11–14)	94.1	94.1	11.5	12.1	16.3
North American boreal (1)	94.0	94.0	11.2	11.7	15.3
North American temperate (2)	87.1	87.1	10.1	11.3	11.7
South American tropical (3)	54.8	54.8	23.0	22.7	19.8
South American temperate (4)	48.3	48.3	17.4	15.9	16.0
Northern Africa (5)	80.5	80.5	7.8	9.8	8.9
Southern Africa (6)	49.0	49.0	18.2	17.3	16.3
Eurasian boreal (7)	96.4	96.4	12.2	12.9	17.5
Asian temperate (8)	90.0	90.0	10.5	12.2	10.2
Asian tropical (9)	87.8	87.8	22.7	23.9	17.3
Australia (10)	48.2	48.2	15.4	13.7	13.4
South-west	90.6	90.6	12.5	12.9	15.8
Europe (11)					
South-east	93.4	93.4	13.8	14.7	18.7
Europe (12)					
North-west	93.5	93.5	15.0	16.0	19.1
Europe (13)					
North-east	93.0	93.0	12.6	13.5	17.5
Europe (14)					
Ocean (16–20)	60.1	60.1	13.7	13.0	9.3

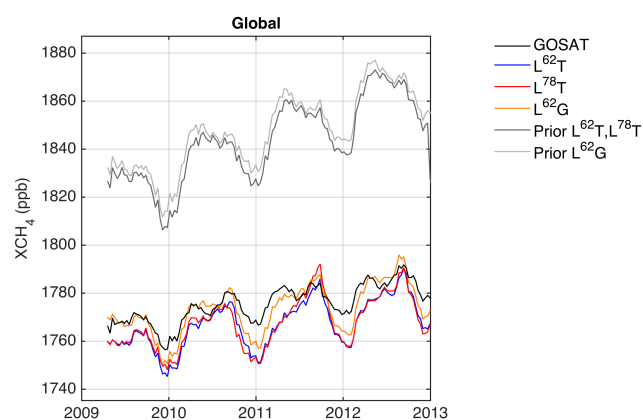


Figure 7. Global GOSAT and simulated regional 10-day mean XCH₄.

3.4 Emission estimates

3.4.1 Global

Our posterior mean total global emission estimate for 2000–2012 is 517 ± 45 Tg CH₄ yr⁻¹ with an increasing trend of 3 Tg CH₄ yr⁻¹ (Table 6, inversion L⁶²G). Posterior mean total global emissions for 2000–2012 are approximately 29 Tg CH₄ yr⁻¹ smaller than the prior (Table 6), although the posterior estimates are within the range of prior uncertainties (± 93 Tg CH₄ yr⁻¹). Posterior mean total global emission estimates from inversions L⁶²T, L⁷⁸T and L⁶²G agree well, and are in line with previous studies, e.g. Bousquet et al. (2006) and Fraser et al. (2013). The main differences in the long-term mean are that anthropogenic mean annual emission estimates in L⁷⁸T are more than 10 Tg CH₄ yr⁻¹ larger than in L⁶²T and L⁶²G, which are compensated by smaller biospheric emissions (Fig. 8). This change in long-term mean flux is not robust in the L⁷⁸ configuration, as the uncertainty is large.

All inversions show an increase in posterior mean total global emissions from before 2007 to after 2007 by 18–19 Tg CH₄ yr⁻¹ (Table 6), which is much smaller than the increase in prior emissions of 33 Tg CH₄ yr⁻¹. The increase in posterior emissions during 2000–2010 is 15–16 Tg CH₄ yr⁻¹ and this agrees well with previous studies by Bergamaschi et al. (2013) and Bruhwiler et al. (2014) for example, who estimated an increase of about 16–20 Tg CH₄ yr⁻¹.

The increase in total global emissions is dominated by the anthropogenic sources in both posterior and prior, and again the increase in the posterior (15–28 Tg CH₄ yr⁻¹) is much less than in the prior EDGAR v4.2 FT2010 inventory (37 Tg CH₄ yr⁻¹) (Fig. 9, Table 6). The posterior anthropogenic emission estimates from 2003–2005 to 2007–2010 increase by 15–23 Tg CH₄ yr⁻¹, which agrees well with Bergamaschi et al. (2013) who estimated an increase of 14–22 Tg CH₄ yr⁻¹. However, the increase in anthropogenic emission estimates is larger than reported by Bruhwiler et al. (2014) who found an increase of around 10 Tg CH₄ yr⁻¹ from 2000–2005 to 2007–2010. The differences between the inversions are partly due to different time periods used, but also due to the use of different sets of observations and prior fluxes. Bergamaschi et al. (2013) used SCIAMACHY satellite-based retrievals and NOAA observations, whereas Bruhwiler et al. (2014) used in situ NOAA discrete and Environment and Climate Change Canada (ECCC) continuous observations. Our study is also based on in situ observations, but includes more discrete and continuous observations globally than the previous two studies. Therefore, estimates from our study could potentially contain important additional information from observations other than those from NOAA and ECCC. In regard to prior emissions, this study and Bergamaschi et al. (2013) used EDGAR v4.2 inventory estimates (the estimates are similar although slightly different versions were used), while Bruhwiler et al. (2014)

Table 6. Mean emission estimates and their uncertainties before and after 2007 ($\text{Tg CH}_4 \text{ yr}^{-1}$). The uncertainties are 1 standard deviation of ensemble distributions. Prior uncertainties are from inversion L^{62}T and L^{62}G . The L^{78}T has larger prior uncertainties in all regions due to its setup. For other regions, see the Supplement. Emission estimates after 2007 that are more than $1 \text{ Tg CH}_4 \text{ yr}^{-1}$ larger than those before 2007 are marked in bold.

Region (mTC)	Total		Anthropogenic		Biospheric	
	Before 2007	After 2007	Before 2007	After 2007	Before 2007	After 2007
Global (1–20)						
Prior	532.9 ± 86.7	566.0 ± 102.6	313.0 ± 80.7	350.5 ± 97.5	172.8 ± 31.6	171.8 ± 31.8
L^{62}T	507.0 ± 45.1	526.3 ± 43.7	287.0 ± 36.4	314.9 ± 34.5	172.8 ± 28.7	167.7 ± 28.7
L^{78}T	508.2 ± 62.0	526.3 ± 60.9	311.4 ± 50.2	326.0 ± 49.7	149.7 ± 45.1	156.6 ± 44.1
L^{62}G	509.1 ± 45.9	527.6 ± 44.0	287.9 ± 37.4	312.2 ± 34.8	174.1 ± 28.8	171.7 ± 28.9
Europe (11–14)						
Prior	56.2 ± 14.2	55.0 ± 14.5	45.4 ± 13.6	45.0 ± 14.1	9.8 ± 3.9	9.0 ± 3.5
L^{62}T	54.2 ± 10.4	51.5 ± 10.5	46.8 ± 10.3	43.8 ± 10.5	6.4 ± 2.7	6.8 ± 2.5
L^{78}T	53.3 ± 13.3	53.3 ± 13.3	45.1 ± 13.4	45.1 ± 13.5	7.2 ± 3.6	7.1 ± 3.4
L^{62}G	59.7 ± 10.6	58.5 ± 10.7	50.9 ± 10.6	49.1 ± 10.7	7.7 ± 2.7	8.4 ± 2.5
North American temperate (2)						
Prior	42.0 ± 20.5	41.9 ± 20.5	33.2 ± 20.3	32.9 ± 20.3	7.7 ± 3.0	7.8 ± 3.0
L^{62}T	49.2 ± 7.7	51.9 ± 6.8	41.8 ± 7.7	45.1 ± 7.0	6.3 ± 2.7	5.7 ± 2.6
L^{78}T	48.4 ± 9.2	48.1 ± 6.8	42.2 ± 9.4	43.1 ± 7.3	5.1 ± 3.7	3.8 ± 3.5
L^{62}G	55.6 ± 8.4	59.1 ± 7.5	47.4 ± 8.4	51.3 ± 7.7	7.2 ± 2.7	6.6 ± 2.7
South American temperate (4)						
Prior	40.0 ± 14.9	42.8 ± 16.0	23.2 ± 13.1	25.5 ± 14.4	14.2 ± 7.0	14.5 ± 6.9
L^{62}T	49.4 ± 14.6	63.3 ± 14.9	28.0 ± 12.9	39.9 ± 13.5	18.8 ± 6.9	20.6 ± 6.7
L^{78}T	51.9 ± 24.6	66.0 ± 24.7	33.6 ± 22.5	46.4 ± 23.0	15.7 ± 9.8	16.9 ± 9.9
L^{62}G	46.0 ± 14.6	58.8 ± 15.0	26.3 ± 12.9	37.9 ± 13.5	17.0 ± 6.9	18.2 ± 6.8
Asian temperate (8)						
Prior	142.4 ± 72.7	164.7 ± 89.8	106.2 ± 72.1	129.3 ± 89.3	34.2 ± 9.6	33.4 ± 9.5
L^{62}T	76.3 ± 24.2	83.7 ± 20.1	36.9 ± 25.0	50.1 ± 20.7	37.4 ± 6.5	31.5 ± 6.1
L^{78}T	66.8 ± 28.7	80.6 ± 24.2	48.4 ± 26.6	54.8 ± 23.2	16.4 ± 24.7	23.8 ± 22.5
L^{62}G	78.2 ± 25.2	81.0 ± 19.9	37.8 ± 26.1	44.2 ± 20.6	38.5 ± 6.9	34.8 ± 6.4
Asian tropical (9)						
Prior	67.7 ± 15.8	70.8 ± 16.6	30.6 ± 8.7	35.7 ± 9.8	31.1 ± 13.2	31.3 ± 13.3
L^{62}T	67.5 ± 14.3	68.3 ± 14.7	32.0 ± 8.4	35.1 ± 9.3	29.6 ± 12.1	29.4 ± 12.1
L^{78}T	69.2 ± 27.8	67.5 ± 28.8	32.2 ± 23.0	32.5 ± 24.7	31.1 ± 19.6	31.3 ± 19.7
L^{62}G	63.2 ± 14.3	65.1 ± 14.8	29.8 ± 8.4	32.8 ± 9.4	27.4 ± 12.2	28.5 ± 12.2

used a constant prior from EDGAR v4.2 for 2000. Although Bergamaschi et al. (2013) found a significant increase in anthropogenic emissions in the constant-prior inversion, the increase was slightly smaller than in their inversions with the trend included in the prior. This could have caused the smaller trend estimated by Bruhwiler et al. (2014), compared to this study.

Biospheric emission estimates in the L^{62}T and L^{62}G inversions after 2007 are slightly smaller than before 2007 (-5 to $-2 \text{ Tg CH}_4 \text{ yr}^{-1}$), following the prior ($-1 \text{ Tg CH}_4 \text{ yr}^{-1}$).

In contrast, L^{78}T shows an increase ($+7 \text{ Tg CH}_4 \text{ yr}^{-1}$). The increase is driven by much smaller biospheric emission estimates in the L^{78}T inversion before 2007, mainly due to significantly smaller biospheric emissions in the temperate Asian region (discussed in Sect. 3.4.3). The small negative trend in biospheric emissions in L^{62}T and L^{62}G is in line with the finding by Bergamaschi et al. (2013). Here, it is again important to note that interannual variability in the CH_4 sink, which could also influence total emissions to the atmosphere, is not included in this study.

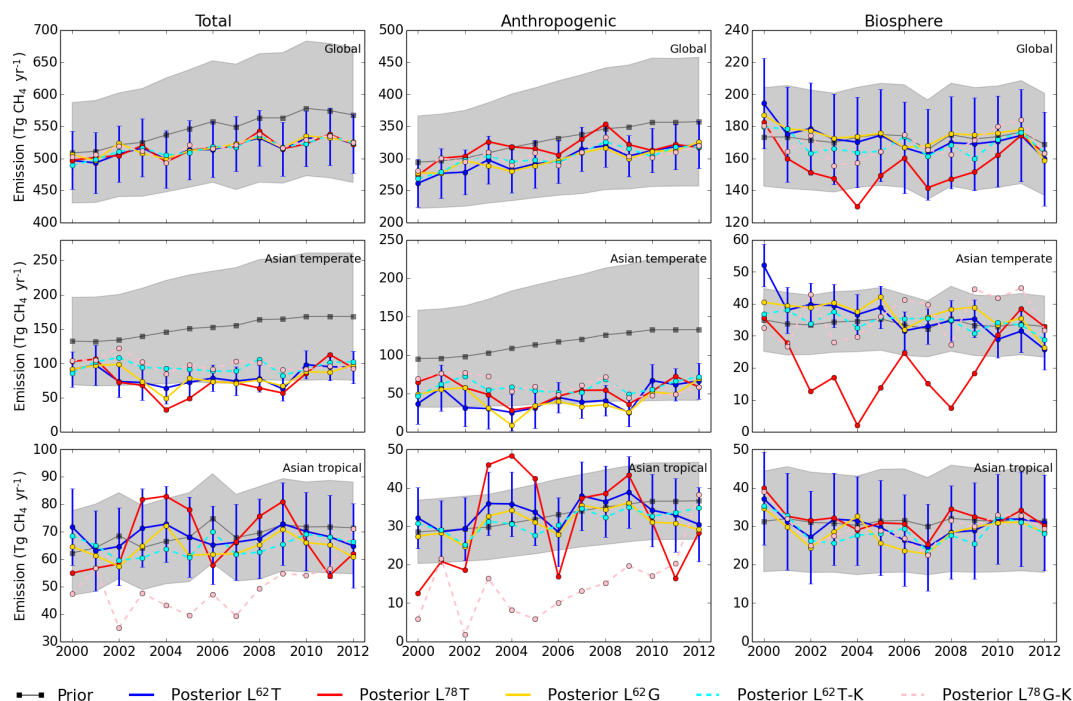


Figure 8. Prior and posterior annual emission estimates for global, Asian temperate and Asian tropical regions. Shaded areas are prior uncertainties, and vertical bars illustrate $L^{62}T$ posterior uncertainties. The uncertainties are 1 standard deviation of ensemble distributions. Note different ranges on the y axes.

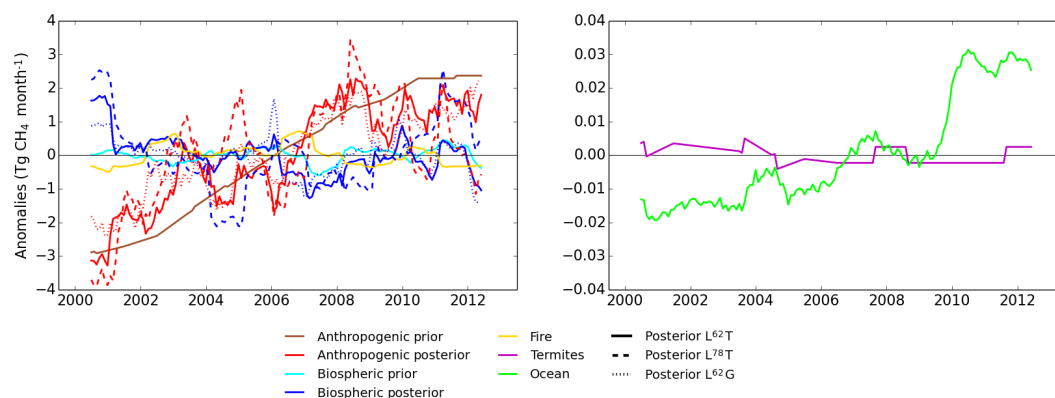


Figure 9. Anomalies of 12-month moving averages of monthly mean emission estimates from five sources. Note that ocean emissions are only from natural sources, i.e. anthropogenic emissions over the ocean are included in anthropogenic emission. Zero levels shown by black lines are the mean of the 2000–2012 moving averages.

3.4.2 Northern Hemisphere boreal regions and Europe

In this section, results for the following mTCs are presented: North American boreal region (mTC1), Eurasian boreal region (mTC7), and Europe (mTC11–14).

Posterior anthropogenic emissions for Europe as a whole (mTC11–14) are similar to the prior ($L^{62}T$, $L^{78}T$) (Table 6), but shifts in the relative contributions to total European emissions from different parts of Europe occurred. Posterior emissions are larger than the prior in southern Europe (south-west

Europe (mTC11) and south-east Europe (mTC12)), whereas the posterior is smaller than the prior in north-east Europe (mTC14) in all inversions (Table S1). Most of the increase in southern Europe and the reduction in north-east Europe are due to anthropogenic emissions. Observed atmospheric CH_4 during winter at many of the in situ sites in northern Europe can be good indicators of anthropogenic signals, because emissions from biogenic sources are small during winter. Posterior atmospheric CH_4 at these sites during winter agrees well with observations, which would indicate

that the posterior anthropogenic emissions are reasonable. Southern Europe is only a small source of biospheric emissions, so most of the atmospheric signals captured at the in situ sites in the region are from anthropogenic sources. In southern Europe, posterior atmospheric CH₄ values at some sites in France, Spain and Italy have a strong positive bias (> 10 ppb), which exceeds the ensemble standard deviations, although the correlations between observed and posterior CH₄ are strong (0.8 or larger). The posterior atmospheric CH₄ values at other sites in south-east Europe are not overestimated, but the correlations are often weaker. This suggests that the inversion did not find a solution that matches all the observations equally, because of an incorrect distribution in the prior within the optimization region. It could also imply that some measurements had local influence that the model could not represent or that the MDM was too small for a few sites. However, the Chi-squared statistics at European sites showed no indication that MDM was too small. Evaluation with aircraft observations shows that vertical transport of CH₄ in Europe is generally good, but evaluation data were only available from central Europe, i.e. we cannot exclude the problem of mixing in the atmosphere elsewhere. Posterior anthropogenic emissions for north-west Europe are similar to the prior. This finding is in line with Bergamaschi et al. (2015), who estimated the anthropogenic emissions in north-west European countries to be similar to the EDGAR v4.2 estimates and larger than the emissions reported in UNFCCC (2013).

For biospheric emission estimates, differences between prior and posterior emissions are negligible in southern Europe (Table S1), whereas the reduction in the posterior is clear in northern Europe (north-west and north-east Europe) (Fig. S8). A reduction in biospheric emissions is also estimated for the North American boreal region (Fig. S8). This suggests that the prior biospheric emissions in boreal regions are too large, which results in larger prior atmospheric CH₄ values than observed. The interannual variability in the posterior emissions also does not follow the prior. An increase in the posterior biospheric emissions is found for 50–90° N in 2006, followed by a decrease until 2010, which is not prominent in the prior. Most of the 2006 increase is from the North American boreal region. This finding does not agree with previous studies, e.g. Bousquet et al. (2011), who found little increase in high northern latitude wetland emissions in 2006. Instead, a significant increase in emissions was found in 2007 in their study. However, observations from specific locations support our findings, although the representativeness of a regional-scale signal is questionable. Moore et al. (2011) reported that 2006 was a warm and wet year at Mer Bleue bog in Canada (45.41° N, 75.48° W), and for the period 2004–2008, the highest autumn CH₄ emissions were observed in 2006. The posterior biospheric emission estimates for north-east Europe in 2006 are about 60 % smaller than the prior estimate in all inversions. Drewer et al. (2010) found that CH₄ emissions in September in Lompolojännkä fen in Fin-

land (67.60° N, 24.12° E) were larger in 2006 than in 2007 due to heavy rain. However, the summer of 2006 was dry with low emissions and snow had already started to fall by the end of September, cutting the emission season short with below zero (°C) temperatures. As such, mean annual CH₄ emissions from the fen were lower in 2006 than in 2007. The high prior emissions in September–October 2006 could be due to a bias in precipitation (excluding snow) and temperature in meteorological data from the Climatic Research Unit (CRU), University of East Anglia, UK (Mitchell and Jones, 2005), which was used as an input for the LPX-Bern model. CRU precipitation and temperature at Lompolojännkä and the mTC14 average are larger than the observations at Lompolojännkä during autumn 2006. The posterior summer biospheric emissions in 2007 are nearly twice as large as the prior. The posterior shows high emissions in July, but the LPX-Bern estimates are low during the summer and autumn at Lompolojännkä and in mTC14 on average. This could be due to problems in the wetland fraction or in the precipitation dependence. CRU precipitation in 2007 is high in early summer and extremely heavy in July at Lompolojännkä and in mTC14 on average, which is in line with Drewer et al. (2010). Although the seasonal cycle of the precipitation is well captured in CRU, if the peatland soil is already saturated with water in early summer, CH₄ emissions would not have increased with additional high summer precipitation. For north-west Europe, similar results are found; posterior biospheric emissions are low in summer–autumn 2006 and high in summer 2007, compared to the prior. The CRU meteorology again agrees well with measurements at Stordalen mire in northern Sweden (68.20° N, 19.03° E) for example, where the measured emissions (Jackowicz-Korczyński et al., 2010) also support the posterior estimates more than the prior.

Differences in emissions between the T1989 and the G2000 convection schemes are prominent in all northern boreal regions and Europe. Posterior emissions in L⁶²G are larger than in L⁶²T and L⁷⁸T throughout 2000–2012. The estimated prior surface atmospheric CH₄ values in these regions are lower when the G2000 scheme is used. This indicates that the stronger vertical transport in the G2000 reduces the surface CH₄ abundance faster than the T1989 scheme and led to larger posterior emissions. We cannot conclude which convection scheme is more suitable for northern boreal regions and Europe based only on the posterior atmospheric CH₄ of those regions, but the agreement with the model-independent aircraft and TCCON retrievals are better in the inversion using the G2000 scheme than in others using the T1989 scheme. Also, van der Veen et al. (2013) found that G2000 more accurately represented vertical transport based on simulations of atmospheric SF₆. Note that the number of available GOSAT retrievals, which agree better with the inversion results using T1989 scheme, is limited for northern Europe, and the retrieval bias (Yoshida et al., 2013) makes the independent information less reliable.

3.4.3 Northern Hemisphere temperate regions

In this section, results for North American (mTC2) and Asian (mTC8) temperate regions are presented.

Posterior total emissions for the North American temperate region are larger than prior emissions in all inversions (Fig. S8, Table 6). The main contribution to the increase in total regional emissions is from anthropogenic emissions. Posterior mean anthropogenic emissions for 2000–2001 are closer to the prior, but nearly $10 \text{ Tg CH}_4 \text{ yr}^{-1}$ larger than the prior for 2004–2012 (Fig. S8). The trend during 2000–2012 is not significant in the prior or in the posterior, although the posterior shows an increase of $0.5 \text{ Tg CH}_4 \text{ yr}^{-1}$ during 2000–2012. The estimated growth rate is similar to the estimates reported by Bruhwiler et al. (2014), but only about one third of that reported by Turner et al. (2016). Our evaluation shows that the trend in posterior XCH_4 matches well with the GOSAT and TCCON retrievals regionally and at sites in the USA, e.g. Park Falls and Oklahoma (Figs. 6, S5, S6). In this study, emissions were optimized by region, and there was only one scaling factor for anthropogenic emission estimates for the North American temperate region. Therefore, it is not possible to study the differences in the emissions trend on the eastern and western sides of the North American temperate region, as in Turner et al. (2016). However, this study suggests that a large increase in local emissions is not necessary to reproduce the increasing atmospheric CH_4 trend. Long-range transport plays a more important role than the local emissions.

A negative correlation is found between mean posterior anthropogenic and biospheric emissions for the North American temperate region, i.e. anthropogenic emissions increased when biospheric emissions decreased. This is an effect of the inversion not being able to separate biospheric and anthropogenic emissions based on the current observational network. In situ observation sites in this area are mostly close to anthropogenic emission sources, so the interannual variability found in biospheric emission estimates may not represent the real variability.

The Asian temperate region has large anthropogenic and biospheric emissions (Table 6). Anthropogenic emissions are responsible for most of the increase in the prior regional and total global emission estimates after 2007. However, prior anthropogenic emissions in this mTC are reduced by more than half in the posterior (Fig. 8, Table 6). Moreover, the increase in posterior anthropogenic emissions for 2000–2012 is not as strong as in the prior (Fig. 8, Table 6). The significant reduction in anthropogenic emissions from prior to posterior estimates for 2002–2010 is driven by observations from two continental sites in Korea; Anmyeon-do (AMY, data available for 2000–2012) and Gosan (GSN, data available for 2002–2011). Small values of MDM were initially assigned and thus the sites had a large impact on the regional flux estimates. When MDMs for those sites are set to 1000 ppb, thereby reducing their influence in the inversion (referred

to as $\text{L}^{62}\text{T-K}$, $\text{L}^{78}\text{G-K}$), the estimated total emission in this mTC is about $30 \text{ Tg CH}_4 \text{ yr}^{-1}$ larger and in better agreement with Bruhwiler et al. (2014) and Bergamaschi et al. (2013) for example.

The increased Asian temperate emissions in simulations $\text{L}^{62}\text{T-K}$ and $\text{L}^{78}\text{G-K}$ are mainly compensated by reduced fluxes in the Asian tropical region (about $10 \text{ Tg CH}_4 \text{ yr}^{-1}$ in L^{62} , about $20\text{--}30 \text{ Tg CH}_4 \text{ yr}^{-1}$ in L^{78}) (Fig. 8), as well as in the Eurasian boreal region, Europe, and the ocean. Only small changes are found in regional emission trends, but the anthropogenic ocean emission estimates in $\text{L}^{62}\text{T-K}$ and $\text{L}^{78}\text{G-K}$ increase less during 2009–2012 compared to that in L^{62}T and L^{78}T . When the two Korean sites are excluded from the inversion, the posterior biospheric emissions in the Asian temperate region remain close to the prior. The interannual variability in total emissions in $\text{L}^{62}\text{T-K}$ and $\text{L}^{78}\text{G-K}$ is smaller than that of L^{62}T and L^{78}G for the Asian temperate region. It is rather unrealistic that regional anthropogenic emissions change by more than $30 \text{ Tg CH}_4 \text{ yr}^{-1}$ over 1 to 2 years as is the case in L^{62}T , L^{78}T , and L^{62}G . Fast growing economies, such as China and India are located in the Asian temperate region, and there is no evidence that the anthropogenic emissions decreased significantly during 2002–2010 in that region. Total emission estimates for the Asian temperate region in $\text{L}^{62}\text{T-K}$ and $\text{L}^{78}\text{G-K}$ are larger and more reasonable than in L^{62}T and L^{78}T , and the ratio of anthropogenic to biospheric emission estimates in $\text{L}^{62}\text{T-K}$ and $\text{L}^{78}\text{G-K}$ are more consistent with each other than in L^{62}T and L^{78}T . This suggests that the L^{62}T and L^{78}T posterior anthropogenic emissions and the L^{78}T posterior biospheric emissions for 2002–2010 are probably unreasonably low due to the influence of the two Asian sites, AMY and GSN. Nevertheless, the posterior emissions in L^{62}T and L^{78}T are lower than in the EDGAR v4.2 FT2010, which is in agreement with previous studies (Pandey et al., 2016; Thompson et al., 2015). The effect of the changes in the emission estimates ($\text{L}^{62}\text{T-K}$ and $\text{L}^{78}\text{G-K}$) to XCH_4 is small, although a slight increase is found globally. The agreements with GOSAT and TCCON XCH_4 in $\text{L}^{62}\text{T-K}$ and $\text{L}^{78}\text{G-K}$ are slightly better for mTCs and at sites where negative biases are found in L^{62}T and L^{78}T (not shown).

3.4.4 Asian and South American tropical regions

In this section, results for the following regions are presented: South American tropical (mTC3) and Asian tropical (mTC9).

The Asian tropical region also has large anthropogenic and biospheric emissions. Prior estimates from both sources are about $30 \text{ Tg CH}_4 \text{ yr}^{-1}$ each, and they are reduced slightly by the inversions (Fig. 8, Table 6). Posterior estimates for biospheric and anthropogenic emissions are lower than in Bruhwiler et al. (2014), who estimated the anthropogenic emissions to be even larger than, and biospheric emissions to be similar to, our prior. The L^{78}T anthropogenic emission es-

timates are lower than the prior estimates due to enhanced, and probably unrealistic, interannual variability compared to the $L^{62}T$ and $L^{62}G$ estimates (Fig. 8). This partly correlates with the strong interannual variability in the Asian temperate region. For example, the increase in anthropogenic emissions in $L^{78}T$ around 2002–2005 is due to a strong decrease in emissions in the Asian temperate region. In the test cases, $L^{62}T-K$ and $L^{78}G-K$, interannual variability in both the Asian temperate and Asian tropical regions is smaller than in $L^{62}T$ and $L^{78}T$ (Fig. 8). However, annual anthropogenic emission estimates in $L^{78}G-K$ are much lower than in $L^{78}T$, and about $20 \text{ Tg CH}_4 \text{ yr}^{-1}$ smaller than in $L^{62}G$. This is partly due to the differences in the convection schemes, which is also seen in the L^{62} configuration. However, it is mostly due to compensating effect of the increased Asian temperate anthropogenic emissions that resulted from reducing the influence of the observations at the Korean sites. Evaluation with surface in situ observations shows that $L^{62}G$ atmospheric CH_4 values agree best with observations at BKT, where the inversions have a strong negative bias. Nevertheless, large uncertainty remains in the estimates, so further information, such as additional observations and prior information about the emissions, is needed to better quantify emissions in this region.

The emission estimates for the South American tropical region are very similar to each other (Fig. S8, Table S1). All posterior emissions are close to the prior, and the uncertainty in the posterior is not reduced by the inversions. This is due to a lack of observations assimilated within the optimization regions in mTC3. Three stations (MEX, KEY, RPB) near the edge of mTC3 were assimilated, but due to strong vertical transport, these observations do not capture signals from tropical wetlands, which is the main CH_4 source from this mTC. Moreover, most of the assimilated observations are samples from well-mixed air masses that represented a large volume of the atmosphere. Therefore, the inversions could not satisfactorily constrain emissions in the South American tropical region.

3.4.5 Africa and southern mid-latitudes

In this section, results for the following regions are presented: South American temperate region (mTC4), northern Africa (mTC5), southern Africa (mTC6) and Australia (mTC10).

Posterior total emissions in the South American temperate region increase significantly during 2006–2009 in all inversions (Fig. S8), and there is no correspondent decrease in other mTCs, e.g. the Asian temperate region. All inversions point in the same direction, but the results are still debatable. Observations assimilated within mTC4 before 2006 are from Ushuaia (USH) in Argentina. Due to its location (54.85° S) having few local emission sources, the purpose of the site is to sample well-mixed air that represents a large volume of the atmosphere. Observations at Arembepe, Brazil (ABP)

were available during 2006–2009, and at Natal, Brazil (NAT) during 2010–2012. These sites capture the well-mixed air in the tropics better than USH, although most of the signals are from the Atlantic Ocean and not from the land. Interannual variability in the tropics is probably better represented by ABP and NAT observations, but it is questionable whether the variability is driven by the observation signals from the South American temperate region. Similar interannual variability was reported by Bruhwiler et al. (2014), where ABP observations were assimilated (the NAT observations were outside their study period), although the changes were not as significant as in this study.

South American temperate is the only region where all inversions show a significant increase in both anthropogenic and biospheric emissions (Table 6). As mTC4 is mostly within 30° S – 30° N , and most of the emissions are located in the northern part of this mTC, the estimates agree with Houweling et al. (2014) who found that most of the increase in total global emissions was in the tropics and the extra-tropics. The increase in emissions during 2005–2008 and the subsequent decrease (Fig. S8) was also found in Basso et al. (2016), who suggested that biospheric emissions from the east part of the Amazon basin were the main contributor to interannual variability. Dlugokencky et al. (2011), using constraints from CH_4 isotopic measurements, suggested emissions from the tropics were an important contributor to the significant growth in atmospheric CH_4 after 2007. The isotopic measurements showed a decrease in the $\delta^{13}\text{C}-\text{CH}_4$, which would indicate that the increased emissions were probably from biogenic sources. The inversions in this study have difficulty changing the ratio of anthropogenic to biospheric emissions from the prior, which could be a reason why the interannual variability of total emissions is optimized by changing emissions from the major sources, i.e. anthropogenic sources. Therefore, interannual variability of the posterior emissions is dominated by the contributions from anthropogenic sources.

Posterior anthropogenic emissions in the northern African and southern African mTCs are larger than the prior for all inversions, with somewhat different interannual variability in the north and south (Fig. S8). Evaluation with in situ observations in northern Africa shows that there is only a small bias in the posterior atmospheric CH_4 values ($< 1 \text{ ppb}$ in $L^{62}G$). For southern Africa, agreement with the in situ observations is good, except for Mt. Kenya, Kenya (MKN) where a strong negative bias is found (see Sect. 3.1). The correlation between the posterior and observed atmospheric CH_4 values at MKN is strong (≥ 0.8), and the site is located at a high altitude ($> 3000 \text{ m a.s.l.}$), which implies that the bias may not be due to small local emissions. On the other hand, vertical transport in the tropics is strong, and MKN is located near a biospheric source area in central Africa. Therefore, the negative bias could also be due to an underestimation of emissions from wetlands in central Africa. Bruhwiler et al. (2014) also reported an increase in the posterior estimates compared

to their prior in Africa, but the increase was mainly in biospheric emissions. However, our interannual variability in anthropogenic emissions in northern Africa is similar to their variability in central African biospheric emission estimates. Therefore, the differences may partly be due to differences in the prior: the ratios of prior anthropogenic to biospheric emissions in this study and Bruhwiler et al. (2014) are almost reciprocals of each other, i.e. our prior anthropogenic emissions are larger and biospheric emissions are lower than in Bruhwiler et al. (2014). It is not possible to conclude from this study which estimates better capture actual emissions, because the estimates for Africa are not well constrained by the observations in either study.

Posterior emissions for Australia in $L^{78}T$ are systematically larger than in $L^{62}T$ and $L^{62}G$ throughout 2000–2012 (Fig. S8). The southernmost coast of Australia and much of New Zealand are defined as “biospheric” land in L^{62} configuration (Fig. S4), i.e. anthropogenic emissions in that optimization region were not optimized in $L^{62}T$ and $L^{62}G$. Since biospheric emissions are a minor source and the posterior emissions changed little from the prior in $L^{78}T$, the “biospheric” land in the land-ecosystem map may need to be changed to “anthropogenic” land for mTC10 to be able to optimize anthropogenic emissions better in $L^{62}T$ and $L^{62}G$.

3.4.6 Ocean

Prior anthropogenic ocean emissions are mainly located in the tropics (mTC20), and the main differences between prior and posterior emissions are also located in this mTC (Fig. S9). All posterior fluxes are 5–10 Tg CH_4 yr^{-1} larger than the prior, especially before 2006 and during 2011–2012 (Fig. S9). However, it is questionable whether these results are reasonable, since there is no indication that non-road transportation and coastal anthropogenic emission estimates varied from year to year as the inversion results show. It is more likely that ocean regions were used to compensate for missing tropical land emissions. Indeed, the estimates for the ocean were sensitive to the estimates in other regions (not shown). Further investigation without optimizing anthropogenic ocean emissions or using only natural ocean emissions as prior, i.e. excluding non-road transport (ship and aircraft) emissions, would help us to better understand the anthropogenic emission estimates over land. Note that the prior biospheric emission estimates in mTC16–20 were not optimized. Prior biospheric emissions around the coast were not zero, partly due to differences in the definition of the coast in the mTC16–20 line in our mTC map and the prior. Only limited information is available in regard to biospheric emissions around coastlines, and as it is a minor source, it was assumed that the inversion would not be able to optimize it.

4 Discussion

4.1 Differences between inversions

Interannual variability of emission estimates is often stronger in $L^{78}T$ than in $L^{62}T$ and $L^{62}G$. Differences are mainly seen in the Asian temperate region, where the proportion of biospheric emissions to total emissions is much smaller in $L^{78}T$ than in $L^{62}T$ and $L^{62}G$. Anthropogenic emission estimates for the Asian tropical region in $L^{78}T$ show strong interannual variability, although the biospheric emission estimates in $L^{78}T$ are similar to the $L^{62}T$ and $L^{62}G$ estimates. The ratio of biospheric to anthropogenic emission estimates in the Asian temperate and Asian tropical regions changes from year to year in $L^{78}T$. The dominant sources are similar in $L^{62}T$ and $L^{62}G$, but sometimes different in $L^{78}T$. For example, in the Asian temperate region, biospheric emissions are larger than anthropogenic emissions during 2003–2005 in $L^{62}T$ and $L^{62}G$, but lower in $L^{78}T$. Only small differences are found in the posterior values of XCH_4 in $L^{62}T$ and $L^{78}T$. Agreement with in situ CH_4 observations is better in $L^{78}T$ than in $L^{62}T$, i.e. the negative bias in the SH is less pronounced in $L^{78}T$. The emission estimates in the SH are often larger in $L^{78}T$ than in $L^{62}T$, where differences are mainly seen in the anthropogenic emission estimates. This means that the land-ecosystem distribution used in this study generally represents the division of the source areas well, although some revision may be needed for Asia and the SH, e.g. Australia.

As expected, interannual variability of emissions in $L^{62}T$ and $L^{62}G$ is similar. This shows that the different convection schemes do not have a large effect on the interannual variability of the emission estimates in L^{62} configuration. The north–south gradient of emissions shows that NH emissions are about 10 Tg CH_4 yr^{-1} larger, and SH emissions about 10 Tg CH_4 yr^{-1} less when the G2000 scheme is used. (Tables 6, S1). In all mTCs, estimates of emissions from the major sources (either biospheric or anthropogenic) are more strongly affected by the convection schemes than the estimates of minor sources ($L^{62}T$ and $L^{62}G$). In $L^{78}T$, the effects of the convection schemes are not assessed in a strictly comparable setup, but similar results are expected (for a fair comparison assessed on a short time period, see Supplement). Note that $L^{78}T$ and $L^{78}G-K$ have significant differences in their annual total emission estimates and their interannual variability in Asian temperate and Asian tropical regions (Fig. 8), but the different convection schemes are not the main cause. Although the emission estimates for the SH are smaller in $L^{62}G$ than in $L^{62}T$, SH posterior surface atmospheric CH_4 and XCH_4 are larger in $L^{62}G$ than in $L^{62}T$, due to faster mixing and larger emission estimates in the NH. Agreement with independent observations is best in $L^{62}G$ among the inversions. NH surface atmospheric CH_4 in $L^{62}G$ is in good agreement with observations at in situ stations, and $L^{62}G$ XCH_4 also agrees best with the TCCON XCH_4 glob-

ally. Although NH XCH₄ in L⁶²G is larger than in GOSAT retrievals, the results suggest that CTE-CH₄ performed better in TM5 when the G2000 scheme is used rather than T1989. It can be assumed that if GOSAT retrievals were assimilated in CTE-CH₄, emission estimates would decrease in the NH and increase in the SH compared to this study. Also, the assimilation of satellite-based retrievals may reduce differences in the estimates between the L⁶²T and L⁶²G setups. However, the assimilation of GOSAT XCH₄ requires further development as previous studies (Houweling et al., 2014; Pandey et al., 2016; Bergamaschi et al., 2013) have shown that the biases in the GOSAT XCH₄ products could misrepresent the distribution and seasonal cycle of the optimized surface emissions.

4.2 Uncertainties in emission estimates

The smallest uncertainties in the posterior total annual emissions are generally seen in L⁶²T, and the largest in L⁷⁸T. We expected that L⁷⁸T would have larger uncertainties than L⁶²T and L⁶²G. The prior uncertainties in L⁷⁸T are the sum of both prior anthropogenic and biospheric uncertainty estimates for each optimization region, whereas the uncertainty in L⁶²T and L⁶²G is from either anthropogenic or biospheric emissions. Although the differences are small (< 0.1 %), uncertainties in the emission estimates in L⁶²G are slightly larger than those in L⁶²T in most of the optimization regions for both anthropogenic and biospheric emissions. It could be that there is more mixing of the surface signals in G2000, thereby producing a wider range of ensemble atmospheric CH₄ values, and thus L⁶²G may have less flux sensitivity at surface sites. However, the difference in the ensemble standard deviation of atmospheric CH₄ values between inversions is small. Furthermore, this cannot be explained by the number of assimilated observations. The uncertainty is larger in L⁶²G than in L⁶²T, while the number of rejected observations is smaller in L⁶²T than in L⁶²G (6.6 and 6.9 %). Similarly, the anthropogenic emission uncertainty is smaller for the Eurasian boreal region than for north-east Europe, which also cannot be explained purely by the number of observations within the region.

For most of the mTCs, anthropogenic emission estimates are larger than biospheric emission estimates, and reductions in uncertainties ($\sigma_r^2 = 1 - \sigma_{\text{posterior}}^2 / \sigma_{\text{prior}}^2$) are also larger for anthropogenic emissions (L⁶²T, L⁶²G). However, for north-east Europe, the reduction in uncertainty for biospheric emission estimates is slightly larger, although the anthropogenic emission estimates are larger than biospheric emissions. This is partly the effect of the land-ecosystem map. Much of north-east Europe is defined as “biospheric” land, i.e. inversions of L⁶²T and L⁶²G can constrain the biospheric estimates more than the anthropogenic estimates. On the other hand, uncertainty reduction in L⁷⁸T is not affected by the land-ecosystem map. Uncertainty reduction rates for biospheric and anthropogenic emission estimates in north-east Europe are similar in L⁷⁸T. Although the posterior uncertain-

ties are largest in the L⁷⁸T estimates, σ_r^2 is also generally the largest in the L⁷⁸T. Note that the Chi-squared statistic for global estimates is 0.9 in L⁶²T, which would indicate that the prior covariance structure is appropriate for this configuration. For L⁷⁸T, the Chi-squared statistic is smaller (0.6), which indicates that the prior state covariance matrix with spatial correlation would probably be more appropriate than the diagonal covariance matrix for this configuration.

Emissions in the Eurasian boreal region are difficult to constrain because of the sparse observation network. Indeed, emissions for mTC7 are estimated not by local observations within the region, but rather by “background” observations that constrain the total budget of a larger area. The only observation site used in this study within mTC7 was Tiksi, Russia (TIK), where observations started in 2010. Although Tiksi is a good reference site for biospheric signals during summer and autumn, one station is not sufficient to constrain the emissions for the whole Eurasian boreal region. Additional observations from the National Institute for Environmental Studies (NIES) tall tower network (Sasakawa et al., 2012) and the Zotino Tall Tower Observatory (ZOTTO) (Winderlich et al., 2010), for example, would be useful to better understand the emissions from this region. Those observations will be included in future studies. Nevertheless, the uncertainties for anthropogenic emissions are reduced by about 20 %, probably due to some influence of observations located in nearby mTCs.

The covariance structure of the posterior estimates is similar to the prior in all inversions. Taken in combination with the Chi-squared statistic (0.9 in L⁶²T), this means either that the assumption in the prior covariance is good, or the inversions are not able to change much from the prior due to, for example, limited prior variation or observation coverage being too sparse. For mTCs such as the South American tropical region, L⁶²T and L⁶²G have a prior correlation between different LETs, but L⁷⁸T shows no correlation between optimization regions. The posterior correlations are similar to the prior in all inversions, i.e. L⁶²T and L⁶²G posterior have a strong correlation; however, L⁷⁸T has almost zero correlation as the dependencies are not well optimized by the inversions. On the other hand, similar posterior correlations between anthropogenic and water optimization regions are found for the Asian temperate mTC region, regardless of the prior assumption. L⁶²T and L⁶²G have a prior correlation of about 0.5, but the correlation is reduced to less than 0.1. L⁷⁸T has a prior correlation of zero, and the posterior correlation does not increase significantly, supporting the L⁶²T and L⁶²G posterior correlation. This suggests that the prior correlation for those optimization regions in L⁶²T and L⁶²G is probably too strong. In the prior covariance, no negative correlation was assumed between any scaling factors. However, some scaling factors are weakly negatively correlated in the posterior estimates. For example, anthropogenic emissions in the Asian temperate region are negatively correlated with those in the Atlantic Ocean in all inversions. This is one of the rea-

sons why ocean emissions are sensitive to the estimates of nearby land regions (see Sect. 3.4.6). The inversions did not turn positive correlations into negative correlations.

5 Summary and conclusions

We presented global and regional CH₄ emissions for 2000–2012 estimated using the CarbonTracker Europe-CH₄ (CTE-CH₄) data assimilation system. Estimates were evaluated against assimilated in situ atmospheric CH₄ observations and model-independent atmospheric measurements from aircraft campaigns, as well as XCH₄ retrievals from TCCON and GOSAT. Three inversions were performed to evaluate the effect of two configurations of CTE-CH₄. The inversions differed by the number of scaling factors and the choice of convection scheme used in the TM5 atmospheric chemistry transport model. One configuration optimized either biospheric or anthropogenic emissions (L^{62}) and the second optimized both (L^{78}) in each optimization region. Interannual variability of the atmospheric CH₄ sink was not taken into account in the inversions. We estimated total global posterior emissions for 2000–2012 at $515\text{--}517 \pm 44\text{--}62 \text{ Tg CH}_4 \text{ yr}^{-1}$. The estimated increase from 2001–2006 to 2007–2012 was $18\text{--}19 \text{ Tg CH}_4 \text{ yr}^{-1}$, which was mainly driven by increased emissions in the modified TransCom (mTC) of the South American temperate, Asian temperate, and Asian tropical regions. This estimated increase in posterior total global CH₄ emissions was more than $10 \text{ Tg CH}_4 \text{ yr}^{-1}$ smaller than in the prior. The inversions suggested that most of the increase was in anthropogenic rather than biospheric emission estimates. However, we could not confirm whether the increase was caused by anthropogenic or biospheric emissions. The inversions had a tendency to optimize regions with major sources, and anthropogenic emission estimates were often larger than biospheric emissions in optimization regions.

Furthermore, posterior emissions were generally smaller than prior emissions in the high latitudes of the NH (North American boreal region, Europe and Eurasian boreal regions), whereas posterior emissions were larger than the prior emissions in Africa and the SH (northern Africa, southern Africa, South American temperate region and Australia). For the tropics (South American tropical and Asian tropical mTC regions), posterior emissions were similar or slightly lower than the prior emissions. This was consistent in all inversions, i.e. the spatial distribution in the prior emissions, probably for anthropogenic sources, may need to be revised with less emissions in the mid-latitude NH and more emissions in temperate regions in the SH.

The study focused on Europe in more detail by dividing it into four mTCs: south-east, south-west, north-east and north-west Europe. Neither prior nor posterior emissions showed any significant trends in anthropogenic or biospheric emission estimates in Europe as a whole. However, the posterior anthropogenic emissions were larger than the estimates in the

EDGAR v4.2 FT2010 inventory for southern Europe, while they were lower in northern Europe. Also, the posterior biospheric emission estimates show different interannual variability than those from the LPX-Bern vegetation model, such that CTE-CH₄ estimates agreed better with CH₄ emissions measured at some wetland sites. Furthermore, the application of different scaling factors to regions divided by land-ecosystem type was an improvement. This approach could be useful to better understand the dependence of CH₄ emissions on meteorological parameters for different ecosystem types, and development of the approach will continue. Posterior emissions in Europe were similar regardless of whether only anthropogenic or biospheric emissions were optimized, or both categories were optimized in each optimization region. Total emissions were similar and the ratio of anthropogenic to biospheric estimates did not change much from the prior.

In the Asian temperate and Asian tropical regions, L^{62} configuration was found to be more consistent with observations, and it produced more reasonable emission estimates. On the other hand, L^{78} configuration was better where both anthropogenic and biospheric emissions were large or the land-ecosystem map was badly defined, such as Australia.

Evaluations with in situ observations showed that the inversions successfully reduced the bias between observed and estimated CH₄ abundance from the prior to the posterior. A comparison with model-independent retrievals of XCH₄ from TCCON and GOSAT showed that agreement in posterior XCH₄ was especially good in the NH. However, negative biases in XCH₄ were found in the SH in all inversions, although the seasonal cycle at the TCCON sites was well captured. This suggests that there are some emissions that were not optimized well by CTE-CH₄, although possible errors in the vertical or stratospheric distributions due to the transport model cannot be ignored. The evaluation also revealed that TM5 with the G2000 convection scheme produces larger emission estimates in the NH and smaller emissions in the SH when compared to the T1989 convection scheme. With the G2000 convection scheme, transport from the NH to the SH was faster, leading to smaller inferred SH emissions and larger NH emissions. This means that the posterior emissions were closer to the prior in the SH than in the NH when the G2000 convection scheme was used. Furthermore, posterior atmospheric CH₄ values agreed slightly better with observations when the G2000 convection scheme was used. In addition, evaluation with GOSAT XCH₄ revealed that the spring peaks in XCH₄ in the tropics were poorly captured in inversions that used the T1989 convection scheme. This feature was best captured in the inversion using the G2000 convection scheme, which estimated larger NH winter emissions than the inversions that used the T1989 convection scheme.

Our key messages include the following findings:

- Global and regional CH₄ emissions for 2000–2012 were estimated using CTE-CH₄ to examine the cause of increase in atmospheric CH₄ after 2007.
- An 18–19 Tg CH₄ yr^{−1} increase in global CH₄ emissions was needed from before 2007 to after 2007 to match the increase in the observed atmospheric CH₄ growth rate of about 6 ppb yr^{−1} (without taking into account interannual variability of the atmospheric CH₄ sink).
- We found the main increase in emissions was located in South American temperate and Asian temperate regions but contributions from either biospheric or anthropogenic sources could not be concluded.
- Agreement of posterior atmospheric CH₄ values with in situ observations and aircraft observations, and of posterior XCH₄ with TCCON and GOSAT retrievals, was good. Agreement was better when the Gregory et al. (2000) convection scheme was used.
- A large increase in anthropogenic CH₄ emissions from temperate North America was not needed to match observations.

Code and data availability. The source code of CTE-CH₄ and data presented in this paper are part of the CTDAS code repository maintained by Wageningen University & Research, and all model results and code will be provided on request from the corresponding author (Aki Tsuruta: Aki.Tsuruta@fmi.fi). TCCON data (Blumenstock et al., 2014; De Mazière et al., 2014; Deutscher et al., 2014; Feist et al., 2014; Griffith et al., 2014a, b; Hase et al., 2014; Iraci et al., 2014; Kawakami et al., 2014; Kivi et al., 2014; Sherlock et al., 2014a, b; Strong et al., 2014; Susstmann and Rettinger, 2014; Wennberg et al., 2014a–e) are available from the TCCON Data Archive, hosted by the Carbon Dioxide Information Analysis Center (CDIAC) at Oak Ridge National Laboratory, Oak Ridge, Tennessee, USA, <http://tccon.ornl.gov>.

The Supplement related to this article is available online at doi:10.5194/gmd-10-1261-2017-supplement.

Acknowledgements. We thank the Nessling foundation, NCoE DEFROST, NCoE eSTICC and the Finnish Academy project CARB-ARC (285630) for their financial support. We thank Akihiko Ito for providing prior emissions of termites, and Lori Bruhwiler for the valuable discussion that greatly assisted this work. We are grateful for the Swiss Federal Laboratories for Materials Science and Technology (EMPA), Environment and Climate Change Canada (ECCC), Meteorological Research Institute (MRI), Laboratoire des Sciences du Climat et de l'Environnement (LSCE), the National Institute of Water and Atmospheric Research Ltd. (NIWA), the Environment Division Global Environment and

Marine Department Japan Meteorological Agency (JMA), National Institute for Environmental Studies (NIES), Umweltbundesamt Germany/Federal Environmental Agency (UBA), Umweltbundesamt Austria/Environment Agency Austria (EAA) as the data provider for Sonnblick, the Southern African Weather Service (SAWS), the Main Geophysical Observatory (MGO), the Korea Meteorological Administration (KMA), Meteorology, Climatology, and Geophysics Agency Indonesia (BMKG), University of Bristol (UNIVBRIS), National Institute of Environmental Research (NIER), and Centre for Environmental Monitoring (RIVM) for performing high-quality CH₄ measurements at global sites and making them available through the GAW-WDCGG. The in situ methane measurements at Lauder, Baring Head, and Arrival Heights are conducted as part of NIWA's government-funded, core research from New Zealand's ministry of Business, Innovation and Employment. The observations by JMA are a part of the GAW program of the WMO. For aircraft measurements of the IMECC project we acknowledge the support of the European Commission within the 6th Framework Program through the Integrated Infrastructure Initiative IMECC (Infrastructure for Measurement of the European Carbon Cycle), and the Max Planck Society for funding additional flight hours onboard the Learjet. For regular aircraft measurements at Bialystok we thank the gas lab at the Max Planck Institute for Biogeochemistry at Jena for analysis of the flask samples, and the Max Planck Society for funding. We also acknowledge the California Institute of Technology, University of Wollongong, Institute of Environmental Physics, University of Bremen, NIWA, NIES, Karlsruhe Institute of Technology, IMK-IFU, Japan Aerospace Exploration Agency (JAXA), Los Alamos National Laboratory, University of Toronto, NASA Ames Research Center, and Max Planck Institute for Biogeochemistry for their XCH₄ retrievals. This work was also supported by the EU-FP7 InGOS project (no. 284274), ICOS Carbon Portal (ICOS-ERIC, no. 281250) and Academy of Finland Center of Excellence (no. 272041).

Edited by: A. Stenke

Reviewed by: two anonymous referees

References

- Azar, C. and Johansson, D. J. A.: On the relationship between metrics to compare greenhouse gases – the case of IGTP, GWP and SGTP, *Earth Syst. Dynam.*, 3, 139–147, doi:10.5194/esd-3-139-2012, 2012.
- Basso, L. S., Gatti, L. V., Gloor, M., Miller, J. B., Domingues, L. G., Correia, C. S. C., and Borges, V. F.: Seasonality and interannual variability of CH₄ fluxes from the eastern Amazon Basin inferred from atmospheric mole fraction profiles, *J. Geophys. Res.-Atmos.*, 121, 168–184, doi:10.1002/2015JD023874, 2016.
- Bates, T. S., Kelly, K. C., Johnson, J. E., and Gammon, R. H.: A reevaluation of the open ocean source of methane to the atmosphere, *J. Geophys. Res.*, 101, 6953–6961, doi:10.1029/95JD03348, 1996.
- Belikov, D. A., Maksyutov, S., Sherlock, V., Aoki, S., Deutscher, N. M., Dohe, S., Griffith, D., Kyrö, E., Morino, I., Nakazawa, T., Notholt, J., Rettinger, M., Schneider, M., Susstmann, R., Toon, G. C., Wennberg, P. O., and Wunch, D.: Simulations of column-

- averaged CO₂ and CH₄ using the NIES TM with a hybrid sigma- θ vertical coordinate, *Atmos. Chem. Phys.*, 13, 1713–1732, doi:10.5194/acp-13-1713-2013, 2013.
- Bergamaschi, P., Frankenberg, C., Meirink, J. F., Krol, M., Dentener, F., Wagner, T., Platt, U., Kaplan, J. O., Körner, S., Heimann, M., Dlugokencky, E. J., and Goede, A.: Satellite cartography of atmospheric methane from SCIAMACHY on board ENVISAT: 2. Evaluation based on inverse model simulations, *J. Geophys. Res.*, 112, D02304, doi:10.1029/2006JD007268, 2007.
- Bergamaschi, P., Houweling, S., Segers, A., Krol, M., Frankenberg, C., Scheepmaker, R. A., Dlugokencky, E., Wofsy, S. C., Kort, E. A., Sweeney, C., Schuck, T., Brenninkmeijer, C., Chen, H., Beck, V., and Gerbig, C.: Atmospheric CH₄ in the first decade of the 21st century: Inverse modeling analysis using SCIAMACHY satellite retrievals and NOAA surface measurements, *J. Geophys. Res.-Atmos.*, 118, 7350–7369, doi:10.1002/jgrd.50480, 2013.
- Bergamaschi, P., Corazza, M., Karstens, U., Athanassiadou, M., Thompson, R. L., Pison, I., Manning, A. J., Bousquet, P., Segers, A., Vermeulen, A. T., Janssens-Maenhout, G., Schmidt, M., Ramonet, M., Meinhardt, F., Aalto, T., Haszpra, L., Moncrieff, J., Popa, M. E., Lowry, D., Steinbacher, M., Jordan, A., O'Doherty, S., Piacentino, S., and Dlugokencky, E.: Top-down estimates of European CH₄ and N₂O emissions based on four different inverse models, *Atmos. Chem. Phys.*, 15, 715–736, doi:10.5194/acp-15-715-2015, 2015.
- Blumenstock, T., Hase, F., Schneider, M., Garcia, O. E., and Sepulveda, E.: TCCON data from Izana (ES), Release GGG2014R0, TCCON data archive, hosted by CDIAC, doi:10.14291/tcon.ggg2014.izana01.R0/1149295, 2014.
- Boucher, O.: Comparison of physically- and economically-based CO₂-equivalences for methane, *Earth Syst. Dynam.*, 3, 49–61, doi:10.5194/esd-3-49-2012, 2012.
- Bousquet, P., Ciais, P., Miller, J. B., Dlugokencky, E. J., Hauglustaine, D. A., Prigent, C., Van der Werf, G. R., Peylin, P., Brunke, E.-G., Carouge, C., Langenfelds, R. L., Lathière, J., Papa, F., Ramonet, M., Schmidt, M., Steele, L. P., Tyler, S. C., and White, J.: Contribution of anthropogenic and natural sources to atmospheric methane variability, *Nature*, 443, 439–443, doi:10.1038/nature05132, 2006.
- Bousquet, P., Ringeval, B., Pison, I., Dlugokencky, E. J., Brunke, E.-G., Carouge, C., Chevallier, F., Fortems-Cheiney, A., Frankenberg, C., Hauglustaine, D. A., Krummel, P. B., Langenfelds, R. L., Ramonet, M., Schmidt, M., Steele, L. P., Szopa, S., Yver, C., Viovy, N., and Ciais, P.: Source attribution of the changes in atmospheric methane for 2006–2008, *Atmos. Chem. Phys.*, 11, 3689–3700, doi:10.5194/acp-11-3689-2011, 2011.
- Brühl, C. and Crutzen, P. J.: MPIC Two-dimensional model, *NASA Ref. Publ.*, 1292, 103–104, 1993.
- Bruhwyler, L., Dlugokencky, E., Masarie, K., Ishizawa, M., Andrews, A., Miller, J., Sweeney, C., Tans, P., and Worthy, D.: CarbonTracker-CH₄: an assimilation system for estimating emissions of atmospheric methane, *Atmos. Chem. Phys.*, 14, 8269–8293, doi:10.5194/acp-14-8269-2014, 2014.
- Dalsøren, S. B., Myhre, C. L., Myhre, G., Gomez-Pelaez, A. J., Søvde, O. A., Isaksen, I. S. A., Weiss, R. F., and Harth, C. M.: Atmospheric methane evolution the last 40 years, *Atmos. Chem. Phys.*, 16, 3099–3126, doi:10.5194/acp-16-3099-2016, 2016.
- Dee, D. P., Uppala, S. M., Simmons, A. J., Berrisford, P., Poli, P., Kobayashi, S., Andrae, U., Balmaseda, M. A., Balsamo, G., Bauer, P., Bechtold, P., Beljaars, A. C. M., van de Berg, I., Biblot, J., Bormann, N., Delsol, C., Dragani, R., Fuentes, M., Greer, A. J., Haimberger, L., Healy, S. B., Hersbach, H., Holm, E. V., Isaksen, L., Kallberg, P., Kohler, M., Matricardi, M., McNally, A. P., Mong-Sanz, B. M., Morcrette, J.-J., Park, B.-K., Peubey, C., de Rosnay, P., Tavolato, C., Thepaut, J. N., and Vitart, F.: The ERA-Interim reanalysis: Configuration and performance of the data assimilation system, *Q. J. Roy. Meteorol. Soc.*, 137, 553–597, 2011.
- De Mazière, M., Sha, M. K., Desmet, F., Hermans, C., Scollas, F., Kumps, N., Metzger, J.-M., Duflot, V., and Cammas, J.-P.: TCCON data from Réunion Island (RE), Release GGG2014R0, TCCON data archive, hosted by CDIAC, doi:10.14291/tcon.ggg2014.reunion01.R0/1149288, 2014.
- Deutscher, N. M., Notholt, J., Messerschmidt, J., Weinzierl, C., Warneke, T., Petri, C., Grupe, P., and Katrynski, K.: TCCON data from Bialystok (PL), Release GGG2014R1, TCCON data archive, hosted by CDIAC, doi:10.14291/tcon.ggg2014.bialystok01.R1/1183984, 2014.
- Dlugokencky, E. J., Masarie, K. A., Lang, P. M., and Tans, P. P.: Continuing decline in the growth rate of the atmospheric methane burden, *Nature*, 393, 447–450, doi:10.1038/30934, 1998.
- Dlugokencky, E. J., Houweling, S., Bruhwiler, L., Masarie, K. A., Lang, P. M., Miller, J. B., and Tans, P. P.: Atmospheric methane levels off: Temporary pause or a new steady-state?, *Geophys. Res. Lett.*, 30, 1992, doi:10.1029/2003GL018126, 2003.
- Dlugokencky, E. J., Bruhwiler, L., White, J. W. C., Emmons, L. K., Novelli, P. C., Montzka, S. A., Masarie, K. A., Lang, P. M., Croftwell, A. M., Miller, J. B., and Gatti, L. V.: Observational constraints on recent increases in the atmospheric CH₄ burden, *Geophys. Res. Lett.*, 36, L18803, doi:10.1029/2009GL039780, 2009.
- Dlugokencky, E. J., Nisbet, E. G., Fisher, R., and Lowry, D.: Global atmospheric methane: budget, changes and dangers, *Philos. T. R. Soc. A*, 369, 2058–2072, doi:10.1098/rsta.2010.0341, 2011.
- Drewer, J., Lohila, A., Aurela, M., Laurila, T., Minkkinen, K., Penttilä, T., Dinsmore, K. J., McKenzie, R. M., Helfter, C., Flechard, C., Sutton, M. A., and Skiba, U. M.: Comparison of greenhouse gas fluxes and nitrogen budgets from an ombrotrophic bog in Scotland and a minerotrophic sedge fen in Finland, *Eur. J. Soil Sci.*, 61, 640–650, doi:10.1111/j.1365-2389.2010.01267.x, 2010.
- Evensen, G.: The Ensemble Kalman Filter: theoretical formulation and practical implementation, *Ocean Dynam.*, 53, 343–367, doi:10.1007/s10236-003-0036-9, 2003.
- Feist, D. G., Arnold, S. G., John, N., and Geibel, M. C.: TCCON data from Ascension Island (SH), Release GGG2014R0, TCCON data archive, hosted by CDIAC, doi:10.14291/tcon.ggg2014.ascension01.R0/1149285, 2014.
- Fraser, A., Palmer, P. I., Feng, L., Boesch, H., Cogan, A., Parker, R., Dlugokencky, E. J., Fraser, P. J., Krummel, P. B., Langenfelds, R. L., O'Doherty, S., Prinn, R. G., Steele, L. P., van der Schoot, M., and Weiss, R. F.: Estimating regional methane surface fluxes: the relative importance of surface and GOSAT mole fraction measurements, *Atmos. Chem. Phys.*, 13, 5697–5713, doi:10.5194/acp-13-5697-2013, 2013.
- Geibel, M. C., Messerschmidt, J., Gerbig, C., Blumenstock, T., Chen, H., Hase, F., Kolle, O., Lavric, J. V., Notholt, J., Palm, M., Rettinger, M., Schmidt, M., Susmann, R., Warneke, T., and Feist, D. G.: Calibration of column-averaged CH₄ over Eu-

- ropean TCCON FTS sites with airborne in-situ measurements, *Atmos. Chem. Phys.*, 12, 8763–8775, doi:10.5194/acp-12-8763-2012, 2012.
- Ghosh, A., Patra, P. K., Ishijima, K., Umezawa, T., Ito, A., Etheridge, D. M., Sugawara, S., Kawamura, K., Miller, J. B., Dlugokencky, E. J., Krummel, P. B., Fraser, P. J., Steele, L. P., Langenfelds, R. L., Trudinger, C. M., White, J. W. C., Vaughn, B., Saeki, T., Aoki, S., and Nakazawa, T.: Variations in global methane sources and sinks during 1910–2010, *Atmos. Chem. Phys.*, 15, 2595–2612, doi:10.5194/acp-15-2595-2015, 2015.
- Giglio, L., Randerson, J. T., and van der Werf, G. R.: Analysis of daily, monthly, and annual burned area using the fourth-generation global fire emissions database (GFED4), *J. Geophys. Res.-Biogeosci.*, 118, 317–328, doi:10.1002/jgrg.20042, 2013.
- Gregory, D., Morcrette, J.-J., Jakob, C., Beljaars, A. C. M., and Stockdale, T.: Revision of convection, radiation and cloud schemes in the ECMWF integrated forecasting system, *Q. J. Roy. Meteorol. Soc.*, 126, 1685–1710, doi:10.1002/qj.49712656607, 2000.
- Griffith, D. W. T., Deutscher, N. M., Velazco, V. A., Wennberg, P. O., Yavin, Y., Keppel Aleks, G., Washenfelder, R., Toon, G. C., Blavier, J.-F., Paton-Walsh, C., Jones, N. B., Kettlewell, G. C., Connor, B., Macatangay, R. C., Roehl, C., Ryzek, M., Glowacki, J., Culfan, T., and Bryant, G.: TCCON data from Darwin (AU), Release GGG2014R0, TCCON data archive, hosted by CDIAC, doi:10.14291/tcon.ggg2014.darwin01.R0/1149290, 2014a.
- Griffith, D. W. T., Velazco, V. A., Deutscher, N. M., Paton-Walsh, C., Jones, N. B., Wilson, S. R., Macatangay, R. C., Kettlewell, G. C., Buchholz, R. R., and Riggenbach, M.: TCCON data from Wollongong (AU), Release GGG2014R0, TCCON data archive, hosted by CDIAC, doi:10.14291/tcon.ggg2014.wollongong01.R0/1149291, 2014b.
- Hase, F., Blumenstock, T., Dohe, S., Gross, J., and Kiel, M.: TCCON data from Karlsruhe (DE), Release GGG2014R1, TCCON data archive, hosted by CDIAC, doi:10.14291/tcon.ggg2014.karlsruhe01.R1/1182416, 2014.
- Heimann, M.: Atmospheric science: Enigma of the recent methane budget, *Nature*, 476, 157–158, doi:10.1038/476157a, 2011.
- Houweling, S., Krol, M., Bergamaschi, P., Frankenberg, C., Dlugokencky, E. J., Morino, I., Notholt, J., Sherlock, V., Wunch, D., Beck, V., Gerbig, C., Chen, H., Kort, E. A., Röckmann, T., and Aben, I.: A multi-year methane inversion using SCIAMACHY, accounting for systematic errors using TCCON measurements, *Atmos. Chem. Phys.*, 14, 3991–4012, doi:10.5194/acp-14-3991-2014, 2014.
- Iraci, L., Podolske, J., Hillyard, P. W., Roehl, C., Wennberg, P. O., Blavier, J.-F., Landeros, J., Allen, N., Wunch, D., Zavaleta, J., Quigley, E., Osterman, G., Barrow, E., and Barney, J.: TCCON data from Indianapolis (US), Release GGG2014R0, TCCON data archive, hosted by CDIAC, doi:10.14291/tcon.ggg2014.indianapolis01.R0/1149164, 2014.
- Ito, A. and Inatomi, M.: Use of a process-based model for assessing the methane budgets of global terrestrial ecosystems and evaluation of uncertainty, *Biogeosciences*, 9, 759–773, doi:10.5194/bg-9-759-2012, 2012.
- Jackowicz-Korczyński, M., Christensen, T. R., Bäckstrand, K., Crill, P., Friborg, T., Mastepanov, M., and Ström, L.: Annual cycle of methane emission from a subarctic peatland, *J. Geophys. Res.*, 115, G02009, doi:10.1029/2008JG000913, 2010.
- Kawakami, S., Ohyama, H., Arai, K., Okumura, H., Taura, C., Fukamachi, T., and Sakashita, M.: TCCON data from Saga (JP), Release GGG2014R0, TCCON data archive, hosted by CDIAC, doi:10.14291/tcon.ggg2014.saga01.R0/1149283, 2014.
- Kirschke, S., Bousquet, P., Ciais, P., Saunio, M., Canadell, J. G., Dlugokencky, E. J., Bergamaschi, P., Bergmann, D., Blake, D. R., Bruhwiler, L., Cameron-Smith, P., Castaldi, S., Chevallier, F., Feng, L., Fraser, A., Heimann, M., Hodson, E. L., Houweling, S., Josse, B., Fraser, P. J., Krummel, P. B., Lamarque, J.-F., Langenfelds, R. L., Le Qué, C., Naik, V., O'Doherty, S., Palmer, P. I., Pison, I., Plummer, D., Poulter, B., Prinn, R. G., Rigby, M., Ringeval, B., Santini, M., Schmidt, M., Shindell, D. T., Simpson, I. J., Spahni, R., Steele, L. P., Strode, S. A., Sudo, K., Szopa, S., van der Werf, G. R., Voulgarakis, A., van Weele, M., Weiss, R. F., Williams, J. E., and Zeng, G.: Three decades of global methane sources and sinks, *Nat. Geosci.*, 6, 813–823, doi:10.1038/ngeo1955, 2013.
- Kivi, R., Heikkinen, P., and Kyrö, E.: TCCON data from Sodankylä (FI), Release GGG2014R0, TCCON data archive, hosted by CDIAC, doi:10.14291/tcon.ggg2014.sodankyla01.R0/1149280, 2014.
- Krol, M., Houweling, S., Bregman, B., van den Broek, M., Segers, A., van Velthoven, P., Peters, W., Dentener, F., and Bergamaschi, P.: The two-way nested global chemistry-transport zoom model TM5: algorithm and applications, *Atmos. Chem. Phys.*, 5, 417–432, doi:10.5194/acp-5-417-2005, 2005.
- Kuze, A., Suto, H., Nakajima, M., and Hamazaki, T.: Thermal and near infrared sensor for carbon observation Fourier-transform spectrometer on the Greenhouse Gases Observing Satellite for greenhouse gases monitoring, *Appl. Opt.*, 48, 6716, doi:10.1364/AO.48.006716, 2009.
- Lambert, G. and Schmidt, S.: Proceedings of the NATO advanced research workshop Reevaluation of the oceanic flux of methane: Uncertainties and long term variations, *Chemosphere*, 26, 579–589, doi:10.1016/0045-6535(93)90443-9, 1993.
- Locatelli, R., Bousquet, P., Chevallier, F., Fortems-Cheney, A., Szopa, S., Saunio, M., Agustí-Panareda, A., Bergmann, D., Bian, H., Cameron-Smith, P., Chipperfield, M. P., Gloor, E., Houweling, S., Kawa, S. R., Krol, M., Patra, P. K., Prinn, R. G., Rigby, M., Saito, R., and Wilson, C.: Impact of transport model errors on the global and regional methane emissions estimated by inverse modelling, *Atmos. Chem. Phys.*, 13, 9917–9937, doi:10.5194/acp-13-9917-2013, 2013.
- McNorton, J., Chipperfield, M. P., Gloor, M., Wilson, C., Feng, W., Hayman, G. D., Rigby, M., Krummel, P. B., O'Doherty, S., Prinn, R. G., Weiss, R. F., Young, D., Dlugokencky, E., and Montzka, S. A.: Role of OH variability in the stalling of the global atmospheric CH₄ growth rate from 1999 to 2006, *Atmos. Chem. Phys.*, 16, 7943–7956, doi:10.5194/acp-16-7943-2016, 2016.
- Meirink, J. F., Bergamaschi, P., and Krol, M. C.: Four-dimensional variational data assimilation for inverse modelling of atmospheric methane emissions: method and comparison with synthesis inversion, *Atmos. Chem. Phys.*, 8, 6341–6353, doi:10.5194/acp-8-6341-2008, 2008.
- Meng, L., Paudel, R., Hess, P. G. M., and Mahowald, N. M.: Seasonal and interannual variability in wetland methane emissions simulated by CLM4Me' and CAM-chem and comparisons to

- observations of concentrations, *Biogeosciences*, 12, 4029–4049, doi:10.5194/bg-12-4029-2015, 2015.
- Michalak, A. M., Hirsch, A., Bruhwiler, L., Gurney, K. R., Peters, W., and Tans, P. P.: Maximum likelihood estimation of covariance parameters for Bayesian atmospheric trace gas surface flux inversions, *J. Geophys. Res.*, 110, D24107, doi:10.1029/2005JD005970, 2005.
- Mitchell, T. D. and Jones, P. D.: An improved method of constructing a database of monthly climate observations and associated high-resolution grids, *Int. J. Climatol.*, 25, 693–712, doi:10.1002/joc.1181, 2005.
- Montzka, S. A., Krol, M., Dlugokencky, E., Hall, B., Jöckel, P., and Lelieveld, J.: Small Interannual Variability of Global Atmospheric Hydroxyl, *Science*, 331, 67–69, doi:10.1126/science.1197640, 2011.
- Moore, T. R., Young, A., Bubier, J. L., Humphreys, E. R., Lafleur, P. M., and Roulet, N. T.: A Multi-Year Record of Methane Flux at the Mer Bleue Bog, Southern Canada, *Ecosystems*, 14, 646–657, doi:10.1007/s10021-011-9435-9, 2011.
- Nisbet, E. G., Dlugokencky, E. J., Manning, M. R., Lowry, D., Fisher, R. E., France, J. L., Michel, S. E., Miller, J. B., White, J. W. C., Vaughn, B., Bousquet, P., Pyle, J. A., Warwick, N. J., Cain, M., Brownlow, R., Zazzeri, G., Lanoisellé, M., Manning, A. C., Gloor, E., Worthy, D. E. J., Brunke, E.-G., Labuschagne, C., Wolff, E. W., and Ganesan, A. L.: Rising atmospheric methane: 2007–2014 growth and isotopic shift, *Global Biogeochem. Cy.*, 30, 1356–1370, doi:10.1002/2016GB005406, 2016.
- Olivié, D. J. L., van Velthoven, P. F. J., Beljaars, A. C. M., and Kelder, H. M.: Comparison between archived and off-line diagnosed convective mass fluxes in the chemistry transport model TM3, *J. Geophys. Res.*, 109, D11303, doi:10.1029/2003JD004036, 2004.
- Pandey, S., Houweling, S., Krol, M., Aben, I., Chevallier, F., Dlugokencky, E. J., Gatti, L. V., Gloor, E., Miller, J. B., Detmers, R., Machida, T., and Röckmann, T.: Inverse modeling of GOSAT-retrieved ratios of total column CH₄ and CO₂ for 2009 and 2010, *Atmos. Chem. Phys.*, 16, 5043–5062, doi:10.5194/acp-16-5043-2016, 2016.
- Peters, G. P., Aamaas, B., Berntsen, T., and Fuglestad, J. S.: The integrated global temperature change potential (iGTP) and relationships between emission metrics, *Environ. Res. Lett.*, 6, 044021, doi:10.1088/1748-9326/6/4/044021, 2011.
- Peters, W., Miller, J. B., Whitaker, J., Denning, A. S., Hirsch, A., Krol, M. C., Zupanski, D., Bruhwiler, L., and Tans, P. P.: An ensemble data assimilation system to estimate CO₂ surface fluxes from atmospheric trace gas observations, *J. Geophys. Res.*, 110, D24304, doi:10.1029/2005JD006157, 2005.
- Peters, W., Jacobson, A. R., Sweeney, C., Andrews, A. E., Conway, T. J., Masarie, K., Miller, J. B., Bruhwiler, L. M. P., Pétron, G., Hirsch, A. I., Worthy, D. E. J., van der Werf, G. R., Randerson, J. T., Wennberg, P. O., Krol, M. C., and Tans, P. P.: An Atmospheric Perspective on North American Carbon Dioxide Exchange: CarbonTracker, *Proc. Natl. Acad. Sci. USA*, 104, 18925–18930, 2007.
- Peters, W., Krol, M. C., Van Der Werf, G. R., Houweling, S., Jones, C. D., Hughes, J., Schaefer, K., Masarie, K. A., Jacobson, A. R., Miller, J. B., Cho, C. H., Ramonet, M., Schmidt, M., Ciattaglia, L., Apadula, F., Heltai, D., Meinhardt, F., Di Sarra, A. G., Piacentino, S., Sferlazzo, D., Aalto, T., Hatakka, J., Ström, J., Haszpra, L., Meijer, H. a. J., Van Der Laan, S., Neubert, R. E. M., Jordan, A., Rodó, X., Morguí, J.-A., Vermeulen, A. T., Popa, E., Rozanski, K., Zimnoch, M., Manning, A. C., Leuenberger, M., Uglietti, C., Dolman, A. J., Ciais, P., Heimann, M., and Tans, P. P.: Seven years of recent European net terrestrial carbon dioxide exchange constrained by atmospheric observations, *Glob. Change Biol.*, 16, 1317–1337, doi:10.1111/j.1365-2486.2009.02078.x, 2010.
- Prather, M. J., Holmes, C. D., and Hsu, J.: Reactive greenhouse gas scenarios: Systematic exploration of uncertainties and the role of atmospheric chemistry, *Geophys. Res. Lett.*, 39, L09803, doi:10.1029/2012GL051440, 2012.
- Prigent, C., Papa, F., Aires, F., Rossow, W. B., and Matthews, E.: Global inundation dynamics inferred from multiple satellite observations, 1993–2000, *J. Geophys. Res.*, 112, D12107, doi:10.1029/2006JD007847, 2007.
- Randerson, J. T., Chen, Y., van der Werf, G. R., Rogers, B. M., and Morton, D. C.: Global burned area and biomass burning emissions from small fires, *J. Geophys. Res.*, 117, G04012, doi:10.1029/2012JG002128, 2012.
- Reisinger, A., Meinshausen, M., Manning, M., and Bodeker, G.: Uncertainties of global warming metrics: CO₂ and CH₄, *Geophys. Res. Lett.*, 37, L14707, doi:10.1029/2010GL043803, 2010.
- Rigby, M., Prinn, R. G., Fraser, P. J., Simmonds, P. G., Langenfelds, R. L., Huang, J., Cunnold, D. M., Steele, L. P., Krummel, P. B., Weiss, R. F., O'Doherty, S., Salameh, P. K., Wang, H. J., Harth, C. M., Mühle, J., and Porter, L. W.: Renewed growth of atmospheric methane, *Geophys. Res. Lett.*, 35, L22805, doi:10.1029/2008GL036037, 2008.
- Rodgers, C. D. and Connor, B. J.: Intercomparison of remote sounding instruments, *J. Geophys. Res.*, 108, 4116, doi:10.1029/2002JD002299, 2003.
- Sanderson, M. G.: Biomass of termites and their emissions of methane and carbon dioxide: A global database, *Global Biogeochem. Cy.*, 10, 543–557, doi:10.1029/96GB01893, 1996.
- Sasakawa, M., Ito, A., Machida, T., Tsuda, N., Niwa, Y., Davydov, D., Fofonov, A., and Arshinov, M.: Annual variation of CH₄ emissions from the middle taiga in West Siberian Lowland (2005–2009): a case of high CH₄ flux and precipitation rate in the summer of 2007, *Tellus B*, 64, 17514, doi:10.3402/tellusb.v64i0.17514, 2012.
- Saunois, M., Bousquet, P., Poulter, B., Peregon, A., Ciais, P., Canadell, J. G., Dlugokencky, E. J., Etiope, G., Bastviken, D., Houweling, S., Janssens-Maenhout, G., Tubiello, F. N., Castaldi, S., Jackson, R. B., Alexe, M., Arora, V. K., Beerling, D. J., Bergamaschi, P., Blake, D. R., Brailsford, G., Brovkin, V., Bruhwiler, L., Crevoisier, C., Crill, P., Covey, K., Curry, C., Frankenberg, C., Gedney, N., Höglund-Isaksson, L., Ishizawa, M., Ito, A., Joos, F., Kim, H.-S., Kleinen, T., Krummel, P., Lamarque, J.-F., Langenfelds, R., Locatelli, R., Machida, T., Maksyutov, S., McDonald, K. C., Marshall, J., Melton, J. R., Morino, I., Naik, V., O'Doherty, S., Parmentier, F.-J. W., Patra, P. K., Peng, C., Peng, S., Peters, G. P., Pison, I., Prigent, C., Prinn, R., Ramonet, M., Riley, W. J., Saito, M., Santini, M., Schroeder, R., Simpson, I. J., Spahni, R., Steele, P., Takizawa, A., Thornton, B. F., Tian, H., Tohjima, Y., Viovy, N., Voulgarakis, A., van Weele, M., van der Werf, G. R., Weiss, R., Wiedinmyer, C., Wilton, D. J., Wiltshire, A., Worthy, D., Wunch, D., Xu, X., Yoshida, Y., Zhang, B., Zhang, Z., and

- Zhu, Q.: The global methane budget 2000–2012, *Earth Syst. Sci. Data*, 8, 697–751, doi:10.5194/essd-8-697-2016, 2016.
- Schaefer, H., Fletcher, S. E. M., Veidt, C., Lassey, K. R., Brailsford, G. W., Bromley, T. M., Dlugokencky, E. J., Michel, S. E., Miller, J. B., Levin, I., Lowe, D. C., Martin, R. J., Vaughn, B. H., and White, J. W. C.: A 21st-century shift from fossil-fuel to biogenic methane emissions indicated by $^{13}\text{CH}_4$, *Science*, 352, 80–84, doi:10.1126/science.aad2705, 2016.
- Schwietzke, S., Sherwood, O. A., Bruhwiler, L. M. P., Miller, J. B., Etiope, G., Dlugokencky, E. J., Michel, S. E., Arling, V. A., Vaughn, B. H., White, J. W. C., and Tans, P. P.: Upward revision of global fossil fuel methane emissions based on isotope database, *Nature*, 538, 88–91, doi:10.1038/nature19797, 2016.
- Sherlock, V., Connor, B., Robinson, J., Shiona, H., Smale, D., and Pollard, D.: TCCON data from Lauder (NZ), 120HR, Release GGG2014R0, TCCON data archive, hosted by CDIAC, doi:10.14291/tcon.ggg2014.lauder01.R0/1149293, 2014a.
- Sherlock, V., Connor, B., Robinson, J., Shiona, H., Smale, D., and Pollard, D.: TCCON data from Lauder (NZ), 125HR, Release GGG2014R0, TCCON data archive, hosted by CDIAC, doi:10.14291/tcon.ggg2014.lauder02.R0/1149298, 2014b.
- Spahni, R., Wania, R., Neef, L., van Weele, M., Pison, I., Bousquet, P., Frankenberg, C., Foster, P. N., Joos, F., Prentice, I. C., and van Velthoven, P.: Constraining global methane emissions and uptake by ecosystems, *Biogeosciences*, 8, 1643–1665, doi:10.5194/bg-8-1643-2011, 2011.
- Spahni, R., Joos, F., Stocker, B. D., Steinacher, M., and Yu, Z. C.: Transient simulations of the carbon and nitrogen dynamics in northern peatlands: from the Last Glacial Maximum to the 21st century, *Clim. Past*, 9, 1287–1308, doi:10.5194/cp-9-1287-2013, 2013.
- Strong, K., Mendonca, J., Weaver, D., Fogal, P., Drummond, J. R., and Lindenmaier, R.: TCCON data from Eureka (CA), Release GGG2014R0, TCCON data archive, hosted by CDIAC, doi:10.14291/tcon.ggg2014.eureka01.R0/1149271, 2014.
- Sussmann, R. and Rettinger, M.: TCCON data from Garmisch (DE), Release GGG2014R0, TCCON data archive, hosted by CDIAC, doi:10.14291/tcon.ggg2014.garmisch01.R0/1149299, 2014.
- Thompson, R. L. and Stohl, A.: FLEXINVERT: an atmospheric Bayesian inversion framework for determining surface fluxes of trace species using an optimized grid, *Geosci. Model Dev.*, 7, 2223–2242, doi:10.5194/gmd-7-2223-2014, 2014.
- Thompson, R. L., Stohl, A., Zhou, L. X., Dlugokencky, E., Fukuyama, Y., Tohjima, Y., Kim, S.-Y., Lee, H., Nisbet, E. G., Fisher, R. E., Lowry, D., Weiss, R. F., Prinn, R. G., O'Doherty, S., Young, D., and White, J. W. C.: Methane emissions in East Asia for 2000–2011 estimated using an atmospheric Bayesian inversion, *J. Geophys. Res. Atmos.*, 120, 4352–4369, doi:10.1002/2014JD022394, 2015.
- Thoning, K. W., Tans, P. P., and Komhyr, W. D.: Atmospheric carbon dioxide at Mauna Loa Observatory: 2. Analysis of the NOAA GMCC data, 1974–1985, *J. Geophys. Res.*, 94, 8549–8565, doi:10.1029/JD094iD06p08549, 1989.
- Tiedtke, M.: A Comprehensive Mass Flux Scheme for Cumulus Parameterization in Large-Scale Models, *Mon. Weather Rev.*, 117, 1779–1800, doi:10.1175/1520-0493(1989)117<1779:ACMFSF>2.0.CO;2, 1989.
- Tsuruta, A., Aalto, T., Backman, L., Peters, W., Krol, M., van der Laan-Luijkx, I. T., Hatakka, J., Heikkinen, P., Dlugokencky, E. J., Spahni, R., and Paramonova, N.: evaluating atmospheric methane inversion model results for Pallas, northern Finland, *Boreal Environ. Res.*, 20, 506–525, 2015.
- Turner, A. J., Jacob, D. J., Benmergui, J., Wofsy, S. C., Maasakkers, J. D., Butz, A., Hasekamp, O., and Biraud, S. C.: A large increase in U.S. methane emissions over the past decade inferred from satellite data and surface observations, *Geophys. Res. Lett.*, 43, 2218–2224, doi:10.1002/2016GL067987, 2016.
- UNFCCC – Secretariat: National greenhouse gas inventory data for the period 1990–2011, Note by the secretariat, Meeting papers on Paris Climate Change Conference, November 2013, SBI 39, United Nations Office at Geneva, Geneva, Switzerland, available at: http://unfccc.int/documentation/documents/advanced_search/items/6911.php?preref=600007639, 2013.
- van der Laan-Luijkx, I. T., van der Velde, I. R., Krol, M. C., Gatti, L. V., Domingues, L. G., Correia, C. S. C., Miller, J. B., Gloor, M., van Leeuwen, T. T., Kaiser, J. W., Wiedinmyer, C., Basu, S., Clerbaux, C., and Peters, W.: Response of the Amazon carbon balance to the 2010 drought derived with Carbon-Tracker South America, *Global Biogeochem. Cy.*, 29, 1092–1108, doi:10.1002/2014GB005082, 2015.
- van der Veen, E.: Optimizing transport properties in TM5 using SF_6 , Wageningen University, University of Twente, Master's thesis, Enschede, the Netherlands, available at: <http://essay.utwente.nl/65459/>, 2013.
- van der Werf, G. R., Randerson, J. T., Giglio, L., Collatz, G. J., Mu, M., Kasibhatla, P. S., Morton, D. C., DeFries, R. S., Jin, Y., and van Leeuwen, T. T.: Global fire emissions and the contribution of deforestation, savanna, forest, agricultural, and peat fires (1997–2009), *Atmos. Chem. Phys.*, 10, 11707–11735, doi:10.5194/acp-10-11707-2010, 2010.
- Wania, R., Ross, I., and Prentice, I. C.: Implementation and evaluation of a new methane model within a dynamic global vegetation model: LPJ-WHyMe v1.3.1, *Geosci. Model Dev.*, 3, 565–584, doi:10.5194/gmd-3-565-2010, 2010.
- Wennberg, P. O., Wunch, D., Roehl, C., Blavier, J.-F., Toon, G. C., and Allen, N.: TCCON data from Caltech (US), Release GGG2014R1, TCCON data archive, hosted by CDIAC, doi:10.14291/tcon.ggg2014.pasadena01.R1/1182415, 2014a.
- Wennberg, P. O., Wunch, D., Yavin, Y., Toon, G. C., Blavier, J.-F., Allen, N., and Keppel-Aleks, G.: TCCON data from Jet Propulsion Laboratory (US), 2007, Release GGG2014R0, TCCON data archive, hosted by CDIAC, doi:10.14291/tcon.ggg2014.jpl01.R0/1149163, 2014b.
- Wennberg, P. O., Roehl, C., Blavier, J.-F., Wunch, D., Landeros, J., and Allen, N.: TCCON data from Jet Propulsion Laboratory (US), 2011, Release GGG2014R0, TCCON data archive, hosted by CDIAC, doi:10.14291/tcon.ggg2014.jpl02.R0/1149297, 2014c.
- Wennberg, P. O., Wunch, D., Roehl, C., Blavier, J.-F., Toon, G. C., Allen, N., Dowell, P., Teske, K., Martin, C., and Martin, J.: TCCON data from Lamont (US), Release GGG2014R1, TCCON data archive, hosted by CDIAC, doi:10.14291/tcon.ggg2014.lamont01.R1/1255070, 2014d.
- Wennberg, P. O., Roehl, C., Wunch, D., Toon, G. C., Blavier, J.-F., Washenfelder, R., Keppel-Aleks, G., Allen, N., and Ayers, J.: TCCON data from Park Falls (US), Release GGG2014R0, TCCON data archive, hosted by CDIAC, doi:10.14291/tcon.ggg2014.parkfalls01.R0/1149161, 2014e.

- Winderlich, J., Chen, H., Gerbig, C., Seifert, T., Kolle, O., Lavric, J. V., Kaiser, C., Höfer, A., and Heimann, M.: Continuous low-maintenance CO₂/CH₄/H₂O measurements at the Zotino Tall Tower Observatory (ZOTTO) in Central Siberia, *Atmos. Meas. Tech.*, 3, 1113–1128, doi:10.5194/amt-3-1113-2010, 2010.
- Wunch, D., Toon, G. C., Blavier, J.-F. L., Washenfelder, R. A., Notholt, J., Connor, B. J., Griffith, D. W. T., Sherlock, V., and Wennberg, P. O.: The Total Carbon Column Observing Network, *Philos. T. Roy. Soc. A*, 369, 2087–2112, doi:10.1098/rsta.2010.0240, 2011.
- Wunch, D., Toon, G. C., Sherlock, V., Deutscher, N. M., Liu, C., Feist, D. G., and Wennberg, P. O.: The Total Carbon Column Observing Network's GGG2014 Data Version, Technical report, Carbon Dioxide Information Analysis Center, Oak Ridge National Laboratory, Oak Ridge, Tennessee, USA, doi:10.14291/tcon.ggg2014.documentation.R0/1221662, 2015.
- Yoshida, Y., Kikuchi, N., Morino, I., Uchino, O., Oshchepkov, S., Bril, A., Saeki, T., Schutgens, N., Toon, G. C., Wunch, D., Roehl, C. M., Wennberg, P. O., Griffith, D. W. T., Deutscher, N. M., Warneke, T., Notholt, J., Robinson, J., Sherlock, V., Connor, B., Rettinger, M., Sussmann, R., Ahonen, P., Heikkinen, P., Kyrö, E., Mendonca, J., Strong, K., Hase, F., Dohe, S., and Yokota, T.: Improvement of the retrieval algorithm for GOSAT SWIR XCO₂ and XCH₄ and their validation using TCCON data, *Atmos. Meas. Tech.*, 6, 1533–1547, doi:10.5194/amt-6-1533-2013, 2013.
- Zhao, C., Andrews, A. E., Bianco, L., Eluszkiewicz, J., Hirsch, A., MacDonald, C., Nehrkorn, T., and Fischer, M. L.: Atmospheric inverse estimates of methane emissions from Central California, *J. Geophys. Res.*, 114, D16302, doi:10.1029/2008JD011671, 2009.